Ozone Retrievals from the Oxygen Infrared Channels of the OSIRIS Infrared Imager

A Thesis
Submitted to the Faculty of Graduate Studies and Research
in Partial Fulfillment of the Requirements
for the Degree of
Master of Science
in the Department of Physics and Engineering Physics

by
J. Truitt Wiensz
Saskatoon, Saskatchewan
June, 2005

To my parents, Ted and Joyce Wiensz.

Abstract

Measurements by OSIRIS, an infrared imaging system that measures emission from excited-state molecular oxygen, are used to retrieve mesospheric ozone through a photochemical model.

The design of the model and the spectral data used in the calculation of photochemical production coefficients are presented. The model has been run in a variety of modes to provide comparisons with measurements of excited-state molecular oxygen; it has been found that the model results are in excellent agreement with measurements.

The model is used in conjunction with a retrieval scheme to estimate the concentrations of mesospheric ozone from measurements made on a satellite platform. An analysis of the sensitivity of retrieved ozone to key model parameters is done, and it is shown that uncertainty in several kinetic reaction rates can significantly change the retrieved results. Comparisons are made for the ozone retrieved in this work and that from several other instruments that make similar measurements. The retrieved concentrations are shown to be in excellent agreement with results from other instruments.

The present work provides a climatological database of mesospheric ozone and will provide useful comparisons with concurrent measurements of mesospheric ozone. The new data obtained in this work are in good agreement with expected results, and it is shown that the unprecedented high-spatial resolution of OSIRIS reveals interesting features that should be further investigated.

Acknowledgements

I would like to express my thanks for the opportunity to perform this work as a member of the Institute of Space and Atmospheric Studies and as a student of the University of Saskatchewan. I further want to thank the Natural Sciences and Engineering Research Council, the Institute, and the University for providing funding for this work.

I would like to express my thanks to a number of individuals within the Institute. My thanks go out to Adam Bourassa, Paul Loewen, and Brad Wilcox, who have been excellent office mates and a pleasure to work alongside. I would like to thank Dr. Nick Lloyd for his helpful comments and conversations throughout the course of my work. I would also like to extend thanks to my faculty supervisors, Dr. Ted Llewellyn and Dr. Doug Degenstein, for their direction throughout this work. I am grateful to Ted Llewellyn for his enthusiasm in his work and his commitment to his students. I want to express appreciation to Doug Degenstein for his dedication to students, commitment to excellence in teaching, and his inspiring approach to science. I am thankful for the opportunity to have worked with such an excellent group of scientists and people.

Finally, I am indebted to my family - Ted and Joyce, Charis and Keith, and Kirsten and Travis - for their constant support and encouragement.

Contents

List of Figures

List of Tables

Glossary of Terms

A-band	Emission of molecular oxygen (762 nm).
A-value	Einstein spontaneous emission coefficient [s^{-1}].
$F(\nu)$	Solar flux $\left[\frac{photons}{cm^2 s}\right]$ at a wavenumber ν.
g-value	Photoexcitation coefficient $\left[\frac{photoexcitations}{s \cdot molecule}\right]$.
h	Planck's constant.
IRIS	InfraRed Imaging System; specifically the three linear array detectors of OSIRIS.
J-value	Photolysis coefficient $\left[\frac{photodissociations}{s \cdot molecule}\right]$.
M	Total atmospheric concentration [cm^{-3}], ([M] $\approx$ [N_2] + [O_2]).
ν	Wavenumber [cm^{-1}].
OIRA	Oxygen InfraRed Atmospheric bands (1.27 μm).
OS	Optical Spectrograph; specifically the UV-visible spectrograph of OSIRIS.
OSIRIS	Optical Spectrograph and InfraRed Imaging System.
Q	Molecule responsible for collisional quenching of an electronically excited molecule.

$\sigma_X(\nu)$	Absorption cross section [cm^2] of molecule X at wavenumber ν.
SME	Solar Mesospheric Explorer.
SZA	Solar zenith angle.
$\tau(\nu)$	Optical depth (dimensionless) at a wavenumber ν.
UV	Ultraviolet
χ	Solar zenith angle at the measurement point.
$[X]$	Volume mixing ratio (parts per million) of a chemical species.
$\mathbf{x}$	Height profile of O_3 concentrations with elements x_i.
$\mathbf{y}$	Height profile of $O_2(a^1\Delta_g)$ concentrations with elements y_j.

Chapter 1

Introduction

1.1 Measurements of Atmospheric Airglow

The study of the airglow - atomic and molecular emissions in the atmosphere - provides a key means of understanding many physical and chemical processes in the atmosphere. Over time an extensive range of measurement techniques and viewing platforms have been developed to study these processes. The dominant measurement technique has passed from ground-based instruments to rocket and balloon measurements through to billion-dollar scientific satellites. Currently the diversity of techniques provides complementary measurements that are made from various measurement platforms. The daily high-resolution global maps of key atmospheric species made with satellite-based instruments are validated by very accurate measurements from dispersed ground-based, balloon, and rocket experiments. The work presented in this thesis employs measurements of the Oxygen InfraRed Atmospheric (OIRA) bands made by the OSIRIS instrument on the Odin satellite. The purpose of this work is to develop a photochemical software model that allows the retrieval of important atmospheric parameters, notably the mesospheric ozone profile, from these OSIRIS measurements.

1.2 The OSIRIS InfraRed Imaging System

OSIRIS, the Optical Spectrograph and InfraRed Imaging System, is the Canadian contribution to the Swedish-led Odin spacecraft. Odin is a collaboration between the Swedish Space Corporation (SSC), the French National Space Board (CNES), the Canadian Space Agency (CSA), and the Finnish Meteorological Institute (FMI). As the name suggests, OSIRIS consists of a UV-visible optical spectrograph and an infrared imaging system. The present work focuses on measurements made by the InfraRed Imaging System (IRIS) of the 1.27 μm emission of molecular oxygen, a key constituent in ozone photochemistry and an important species in the energetics of the mesosphere.

1.3 Photochemical Modeling and Retrieval of Ozone

The chemical species responsible for the 1.27 μm emission of molecular oxygen, $O_2(a^1\Delta_g)$, is primarily produced in the atmosphere when a solar UV photon breaks apart an ozone molecule. As such, daytime measurement of $O_2(a^1\Delta_g)$ serves as a proxy measurement of ozone. In this work, a photochemical software model that estimates the expected height profile of $O_2(a^1\Delta_g)$ concentrations for a given O_3 height profile at a given local time and geographic location has been developed. An investigation of the accuracy of this model is made, and a number of comparisons between measured and modeled $O_2(a^1\Delta_g)$ are presented.

The photochemical model is used in conjunction with a retrieval technique to perform retrievals of mesospheric ozone from $O_2(a^1\Delta_g)$ measured by OSIRIS. A summary of several common retrieval techniques employed in atmospheric remote sensing is presented. Due to the Odin orbit, OSIRIS measurements of $O_2(a^1\Delta_g)$ are made at a variety of local times with sunrise or sunset conditions present throughout roughly a third of the $O_2(a^1\Delta_g)$ measurements. This corresponds to an accelerating and decelerating production of $O_2(a^1\Delta_g)$ from ozone photolysis, and presently limits

the regions of the Odin orbit in which O_3 retrievals can be performed. An investigation of those regions of the Odin orbit that exist in photochemical steady-state conditions is done. Following a brief sensitivity analysis to model parameters, retrieved ozone for a number of times throughout the Odin mission are shown. Several notable features that have been observed are also identified.

1.4 Outline

A history of the measurement of ozone and the oxygen infrared atmospheric bands is given in Chapter 2. Aspects of ozone production and $O_2(a^1\Delta_g)$ photochemistry that are relevant to this work are presented. The OSIRIS instrument is presented in its relation to measurements of the OIRA bands. The Odin orbit and its effects on $O_2(a^1\Delta_g)$ measurements are also discussed.

The photochemical model developed in this work is presented in Chapter 3. Essential elements of photochemical modeling are discussed, namely the solution of the continuity equation, the calculation of photolysis and photoexcitation coefficients, and the penetration depth of solar radiation. The modeled $O_2(a^1\Delta_g)$ for a number of test cases is shown. Various types of retrieval techniques that were considered in this work are outlined in Chapter 4. Local time variations throughout the Odin orbit are used to define regions of the orbit in which ozone retrievals can be performed. A brief analysis of the sensitivity of ozone retrievals to a number of model parameters is given in Chapter 5. It is shown that uncertainty in several key parameters can create significant uncertainty in the retrieved ozone. Comparisons are done between ozone retrieved in this work and ozone retrieved from other instruments. This is followed by a brief presentation of interesting features seen in the retrieved ozone concentrations. A summary of the present work and recommendations for future work are given in Chapter 6.

Chapter 2

Background

2.1 Introduction

This chapter provides an introduction to the measurement and photochemistry of atmospheric $O_2(a^1\Delta_g)$. A summary of its measurement, from discovery to the present day, is presented and followed by a discussion of the photochemical production and loss mechanisms. With this foundation, a description of the OSIRIS instrument is given, and the chapter concludes with a discussion of the OSIRIS measurements of the Oxygen InfraRed Atmospheric bands.

2.2 Ozone

The presence of ozone in the atmosphere was first suggested by Hartley (1880) who, having measured the ultraviolet absorption of ozone, suggested it was responsible for the sharp cutoff in solar irradiance in the ultraviolet region at the ground. Subsequent measurements by Fabry and Buisson (1913, 1921) proved that this was the case, and resulted in the calculation of an ozone column of 0.3 cm, which is very close to current measurements. Chapman (1930) proposed a kinetic model for the production and destruction of atmospheric ozone that still forms the basis of the

current understanding. Chapman stated that ozone formation is initiated by the photolysis of molecular oxygen,

$$O_2 + h\nu(\lambda < 242 \text{ nm}) \longrightarrow O + O, . \tag{2.1}$$

The highly reactive atomic oxygen then reacts with O_2 to form O_3:

$$O + O_2 + M \longrightarrow O_3 + M, \tag{2.2}$$

where the third body M, required to preserve energy and momentum, may be N_2 or O_2. In the Chapman ozone chemistry, photodissociation also plays a role in the cycling between ozone and atomic oxygen; this is seen in the following reaction,

$$O_3 + h\nu(\lambda < 310 \text{ nm}) \longrightarrow O_2 + O, \tag{2.3}$$

where the atomic oxygen product may recombine to produce ozone. To limit the production of ozone by O_2 photolysis, Chapman proposed that 'odd oxygen' (O_x =O+O_3) would be lost through odd-oxygen recombination:

$$O_3 + O \longrightarrow O_2 + O_2. \tag{2.4}$$

The basic Chapman concept assumes a pure oxygen chemistry, with no surface chemistry or catalysis, and no transport. This set of reactions explained the existence of an ozone number density maximum in the stratosphere, as photolysis increases with height and O_2 number density decreases with height. However, the measured rate constant for reaction (2.4) is smaller than that suggested by Chapman, so that oxygen atmosphere scheme would result in larger odd oxygen concentrations than are observed. Further studies (Bates and Nicolet, 1950) showed the existence of catalytic loss cycles in this reaction. These were found to match the calculated ozone abundances to the measured values. However, the assumption of zero transport that was accepted in the original Chapman model would still result in a much greater accumulation of ozone in the tropics than has been observed.

2.3 Measurement of the Oxygen Infrared Atmospheric Bands

An understanding of the photochemistry of atmospheric $O_2(a^1\Delta_g)$ is essential in considering the problem of mesospheric ozone retrieval from OSIRIS observations.

The first observations of the 1.27 μm infrared bands of molecular oxygen were reported by Ellis and Kneser (1933) who measured the absorption spectrum of liquid oxygen. The first reported measurement of these bands in the solar spectrum was made by Herzberg (1934) who used a photographic plate to measure the infrared solar spectrum. Well-resolved fine structure was observed and a detailed fine structure analysis was done to obtain the selection rules and preliminary spectroscopic coefficients for the transition. This analysis revealed that the absorption feacture was due to a (0,0) transition between the singlet delta excited state and the ground state of molecular oxygen.

Subsequently, measurements of the Meinel OH vibrational-rotational bands using ground-based spectrometers (Vallance Jones and Harrison, 1958) revealed an apparent asymmetry in the (4,2) band structure, and led to the discovery of a 1.58 μm oxygen emission. This emission is due to the transition from the zeroth vibrational level of $O_2(a^1\Delta_g)$ to the first vibrational level of ground state molecular oxygen. It was observed that the emission had a steady daytime value and had a decay time of 30 minutes in the evening twilight. The suggested production mechanisms for $O_2(a^1\Delta_g)$ were resonant phosphorescence by infrared solar radiation and the reaction of atomic oxygen and ozone. The initial ground-based observations of the 1.27 μm band were unsuccessful due to the large amount of self-absorption by ground-state molecular oxygen. Self-absorption in the (0,1) band from the emission point to the ground is negligible as the number of O_2 molecules in the first vibrationally excited state is several orders of magnitude less than the number in the zeroth vibrational state. As such, ground-based observations of the (0,1) band yield greater intensities than those of the (0,0) band, at least for observations at low solar

elevation angles.

A series of ground-based observations of the 1.58 μm emission was continued, where work focused on quantifying the daytime emission and the morning and evening twilight variations of the signal. Extensive work by Vallance Jones and Gattinger (1963) suggested that neither of the proposed production mechanisms could satisfactorily explain the existence of $O_2(a^1\Delta_g)$ in the atmosphere. These measurements indicated a seasonal variation in the evening twilight emission when the sun was just above the horizon; the intensity measured in winter was greater, by a factor of three, than the summer emission measurements. However, no such seasonal variation was observed in high-altitude aircraft-based observations of the daytime emission intensity (Gattinger and Vallance Jones, 1966). In the ground-based observations, the 1.58 μm oxygen emission was clearly seen in the evening twilight, but was essentially absent in the morning twilight. To explain this behaviour, Vallance Jones and Gattinger (1963) proposed that the primary production mechanism of $O_2(a^1\Delta_g)$ was the photodissociation of ozone in the Hartley continuum. Collisional quenching of the excited molecules by molecular oxygen, molecular nitrogen, and atomic oxygen was suggested as the cause of the observed twilight decay being less than the radiative lifetime.

As the 1.58 μm band of the oxygen infrared atmospheric bands is blended with the (4,2) band of the Meinel OH system, airborne measurements of the 1.27 μm emission were undertaken to understand the production and loss of the observed $O_2(a^1\Delta_g)$. Noxon and Vallance Jones (1962) made the first reported measurements of the 1.27 μm emission from a high-altitude aircraft, at 13 km. Measurements of the daytime and evening twilight aiglow emissions were made with a grating spectrometer; these showed a daytime zenith emission intensity of 10 MRayleighs. A series of measurements (Noxon and Markham, 1963; Gattinger and Vallance Jones, 1966; Noxon, 1967) made similar aircraft-based observations of the day and twilight emissions of the (0,0) band during a solar eclipse; these results were all consistent with $O_2(a^1\Delta_g)$ production due to ozone photolysis.

Several experiments by Evans (1967) employed a balloon platform to reach an altitude of 30 km; this significantly reduced the amount of self-absorption of the signal. These observations examined the variation of the emission intensity during the morning and evening twilight periods and throughout the day. Measurements were also made during the daytime ascent of the balloon to assess the contribution of resonance phosphorescence; these showed that there was no significant volume emission below 30 km and led to its rejection as a primary source of atmospheric $O_2(a^1\Delta_g)$. These observations also showed several key trends: a rapid increase in emission intensity throughout the morning twilight, when ultraviolet radiation first reaches the region of the ozone maximum; a dayglow variation that suggests photochemical equilibrium; and a slower decay of the signal in the evening twilight than that observed from ground-based measurements.

The balloon experiments demonstrated that the bulk of the 1.27 μm emission originated above 30 km, but said little about the altitude distribution of the emission. A series of rocket experiments (Llewellyn *et al.*, 1967; Evans *et al.*, 1968) showed that the emission peaked near an altitude of 55 km, and confirmed that the production of atmospheric $O_2(a^1\Delta_g)$ is primarily due to ozone photolysis. A distinct second layer in the emission profile near 85 km was observed during the course of these experiments. Additional rocket-based experiments (Haslett *et al.*, 1969; Wood, 1972) made similar observations, and so confirmed the existing observations and understanding.

At that time, the use of satellite technology to obtain global maps of atmospheric constituents had spread to the public research sector. Global maps of singlet delta observations were made possible by the Solar Mesospheric Explorer (SME), which made measurements of the 1.27 μm band with a limb-scanning spectrometer, together with measurement of ozone in the stratosphere and mesosphere. SME observations confirmed the excess emission above 80 km reported by Evans *et al.* (1968), and provided evidence to support the claim that this excess was an ozone feature (Thomas *et al.*, 1983; Thomas *et al.*, 1984).

As the ability to make global measurements with satellites improved, and with the detailed height resolution made possible by rocket experiments, there was need for a greater understanding of the production and loss mechanisms of atmospheric $O_2(a^1\Delta_g)$. With this goal in mind, modeling work was performed over the next several years; this focused on better interpretation of observations, notably the non-steady state twilight observations. Several photochemical models were developed to aid in the interpretation of measurements (López-González, 1989; Sica, 1991; Mlynczak and Olander, 1995). The standard model for $O_2(a^1\Delta_g)$ was developed by Mlynczak *et al.* (1993).

OSIRIS is one of a series of recent satellite-borne instruments that make global measurements of $O_2(a^1\Delta_g)$, along with NASA's SABER on TIMED (Russel *et al.*, 1999), and the European Space Agency's SCIAMACHY on ENVISAT (Bovensmann *et al.*, 1999). However, a distinguishing feature is that OSIRIS makes use of a tomographic technique that provides unprecedented spatial resolution in measurements of the 1.27 μm emission (Degenstein *et al.*, 2003).

2.4 Photochemistry of $O_2(a^1\Delta_g)$

The (0,0) band of the Oxygen InfraRed Atmospheric (OIRA) band system at 1.27 μm is one of the brightest emissions in the airglow. The emission results from a vibrational-rotational spin-forbidden magnetic dipole transition in molecular oxygen,

$$O_2(a^1\Delta_g) \longrightarrow O_2(X^3\Sigma_g^-) + h\nu(1.27\mu\text{m}). \tag{2.5}$$

Due to the magnetic dipole nature of this transition, and so its relatively low transition probability, the emission has a long radiative lifetime; the spontaneous emission coefficient (A_Δ) is $2.19 \times 10^{-4}\ s^{-1}$ (Newman *et al.*, 1999).

The key photochemical processes involved in the production and loss of $O_2(a^1\Delta_g)$ are illustrated in Figure 2.1. All branches and mechanisms mentioned in the following discussion refer to the mechanisms shown in this figure.

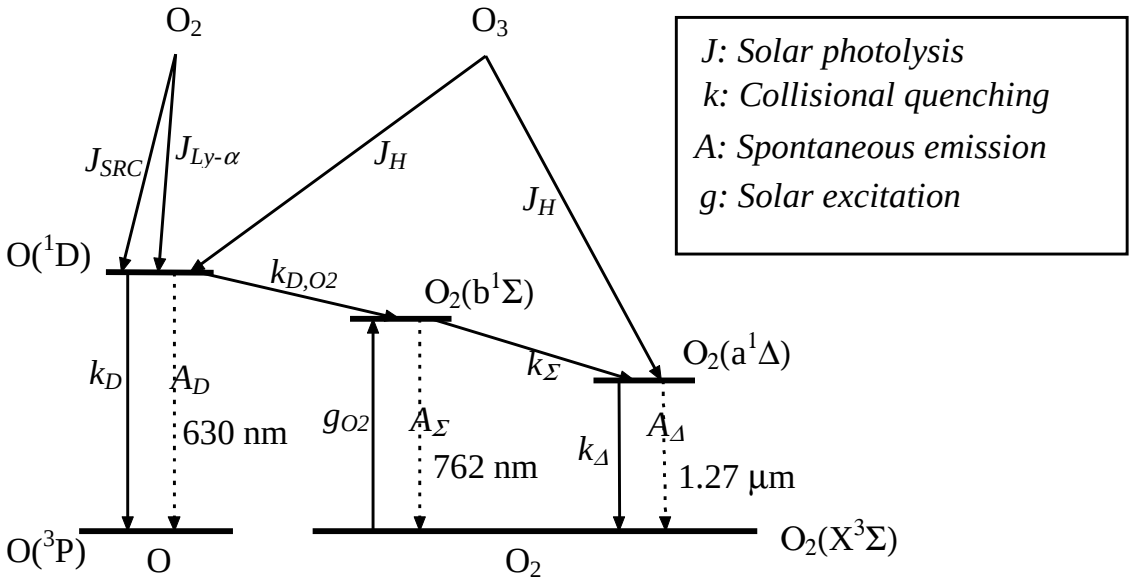

Figure 2.1: Production and loss mechanisms for $O_2(a^1\Delta_g)$.

Ozone photodissociation, J_H, is the primary production mechanism for $O_2(a^1\Delta_g)$. Ozone photolysis in the Hartley band results in $O_2(a^1\Delta_g)$ as well as excited atomic oxygen, $O(^1D)$:

$$O_3 + h\nu(210 - 310 \text{ nm}) \longrightarrow O_2(a^1\Delta_g) + O(^1D), \tag{2.6}$$

with a quantum efficiency of $\phi = 0.9$.

In addition to direct production through ozone photolysis, $O_2(a^1\Delta_g)$ is also produced indirectly by energy transfer (k_{D,O_2}) from $O(^1D)$ by way of $O_2(b^1\Sigma_g^+)$. In this process, $O(^1D)$ reacts with O_2, transferring energy to the molecule that results in the formation of the excited $O_2(b^1\Sigma_g^+)$ state,

$$O(^1D) + O_2 \longrightarrow O_2(b^1\Sigma_g^+) + O(^3P). \tag{2.7}$$

In turn, $O_2(b^1\Sigma_g^+)$ interacts with other molecules, and is quenched (k_Σ) to $O_2(a^1\Delta_g)$,

$$O_2(b^1\Sigma_g^+) + Q \longrightarrow O_2(a^1\Delta_g) + Q, \tag{2.8}$$

where the quencher Q in this reaction may be one of several atmospheric molecules (CO_2, O_3, O, O_2, or N_2). In addition to the production of $O_2(b^1\Sigma_g^+)$ through energy transfer from $O(^1D)$ (2.7), it is also produced by the direct resonant absorption of sunlight at 762 nm,

$$O_2 + h\nu(762 \text{ nm}) \longrightarrow O_2(b^1\Sigma_g^+). \tag{2.9}$$

In addition to the radiative relaxation of $O_2(a^1\Delta_g)$ (2.5), there is also collisional quenching (k_Δ),

$$O_2(a^1\Delta_g) + Q \longrightarrow O_2(X^3\Sigma_g^-) + Q. \tag{2.10}$$

At lower altitudes, where the atmospheric density is large, collisional quenching is the dominant factor in determining the average lifetime of a $O_2(a^1\Delta_g)$ molecule. The altitude dependence of the chemical lifetime of $O_2(a^1\Delta_g)$, as calculated by the model developed in this work, is shown in Figure 2.2. It is apparent that below about

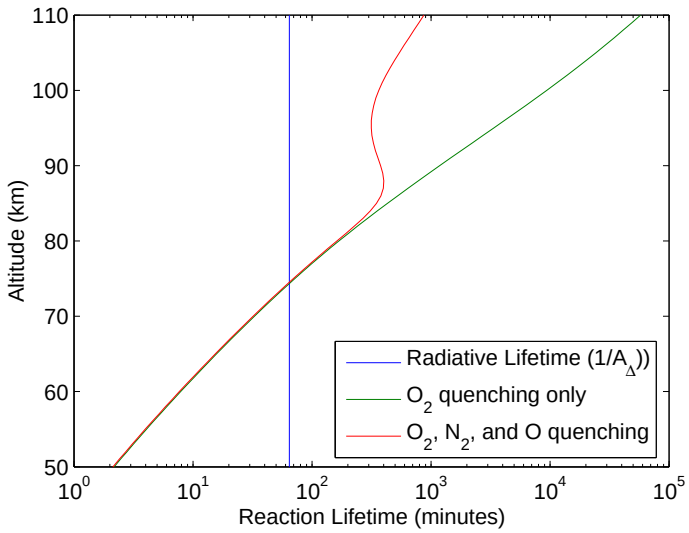

Figure 2.2: Height dependence of $O_2(a^1\Delta_g)$ lifetime.

75 km, where the quenching lifetime is much shorter than the radiative lifetime, it is increasingly likely that a $O_2(a^1\Delta_g)$ molecule will quench to the ground state before it can radiate.

In addition to production by ozone photolysis (J_H), O(^{1}D) is also produced in the photodissociation of molecular oxygen in the Schumann-Runge continuum (J_{SRC}), and by Lyman alpha ($J_{Ly-\alpha}$)

$$O_2 + h\nu(\mathrm{SRC}, \mathrm{Ly}{-}\alpha) \longrightarrow O(^3P) + O(^1D). \tag{2.11}$$

Both $O_2(b^1\Sigma_g^+)$ and O(^{1}D) can radiatively decay, with radiation lifetimes of 12 s and $\sim$2 minutes respectively.

The presence of strong high-altitude 1.27 μm emissions visible in the absence of solar illumination has suggested an additional atmospheric $O_2(a^1\Delta_g)$ production mechanism (Bantle *et al.*, 1984). It is generally accepted that this source is a three body recombination of atomic oxygen,

$$O(^3P) + O(^3P) + M \longrightarrow O_2(a^1\Delta) + M. \tag{2.12}$$

This 'nightglow' layer, which is typically observed at a range of heights centered around 90 km, is located within the region of the atomic oxygen maximum.

2.5 Features of the Oxygen Infrared Atmospheric Bands

The energy levels and transitions relating to the lowest excited states of molecular oxygen are shown in Figure 2.3. It should be noted that the $O_2(C^3\Delta_u^+)$ state is also known as the $O_2(A^3\Delta_u^+)$ state. The selection rules for the $O_2(a^1\Delta_g)$ to ground-state spin-forbidden magnetic dipole transition govern the observed emission. The selection rules require that $\Delta K = 0, \pm 1, \pm 2$, $\Delta J = 0, \pm 1$, and that symmetric states combine with symmetric states (Herzberg, 1989). The nine branches of the transition, as allowed by the selection rules, are shown in Figure 2.4. It should be noted that the zero nuclear spin of molecular oxygen means that certain rotational levels are absent; these missing levels are shown as dotted in the figure. The absorp-

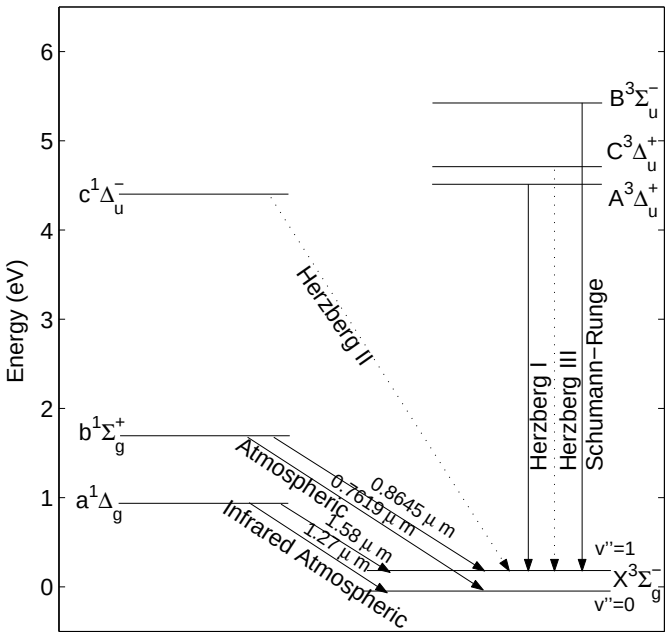

Figure 2.3: Electronic states and transitions of O_2.

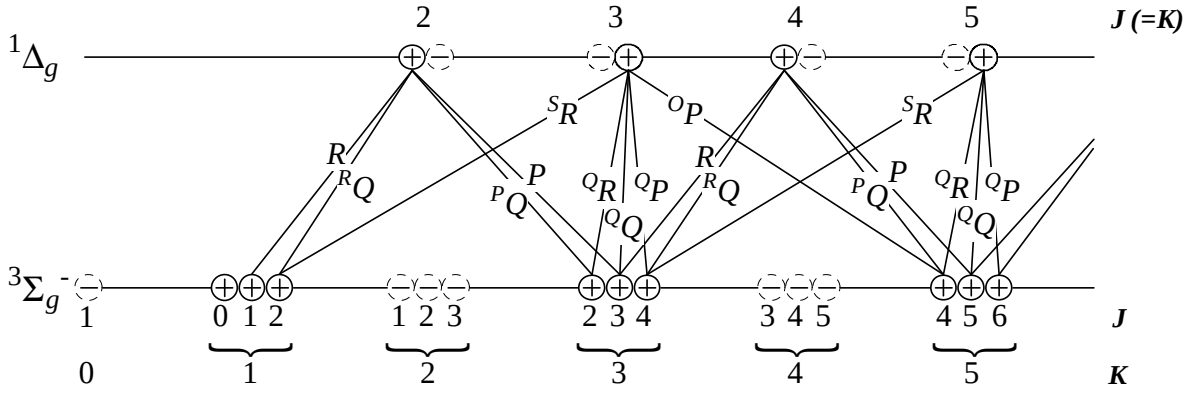

Figure 2.4: Branches of the $O_2(a^1\Delta_g - X^3\Sigma_g^-)$ bands.

tion cross section for the $O_2(a^1\Delta_g)$ to ground state transition, calculated using line positions and line strengths from the HITRAN database (Rothman *et al.*, 2003), is shown in Figure 2.5. The lines in this figure have a finite width that cannot be seen on this scale. Radiation in the oxygen infrared atmospheric bands is also possible through an electric quadrupole transition, however the contribution by the quadrupole term to the transition probability is expected to be several orders of magnitude less than that for the magnetic dipole term (Herzberg, 1989).

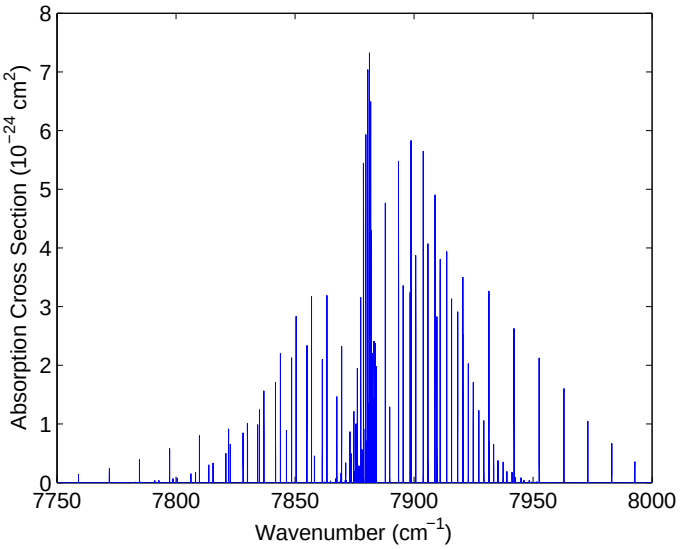

Figure 2.5: Absorption cross section of the $O_2(a^1\Delta_g - X^3\Sigma_g^-)$ bands.

2.6 The Odin Spacecraft

The Odin spacecraft is a collaboration between the Swedish, Canadian, French, and Finnish space science communities. Odin was launched on February 20, 2001, from the Svobodny Cosmodrome in eastern Siberia (51°23'N,128°08'E) into a near-terminator sun-synchronous orbit. The Odin orbit is at an inclination of 97.8° to the equatorial plane, leading to a precession period of 365 days, with the ascending

node at 1800 LST (Local Solar Time). The Odin orbital period is 96 minutes, and as such the longitude changes by 24° on successive orbits. The illuminated latitudinal coverage varies throughout the year, and has limiting values of 82.2° S and 82.2° N. The relative orientation of the Odin orbit to the sun at several times throughout the year are shown in Figure 2.6. Odin carries two instruments, OSIRIS

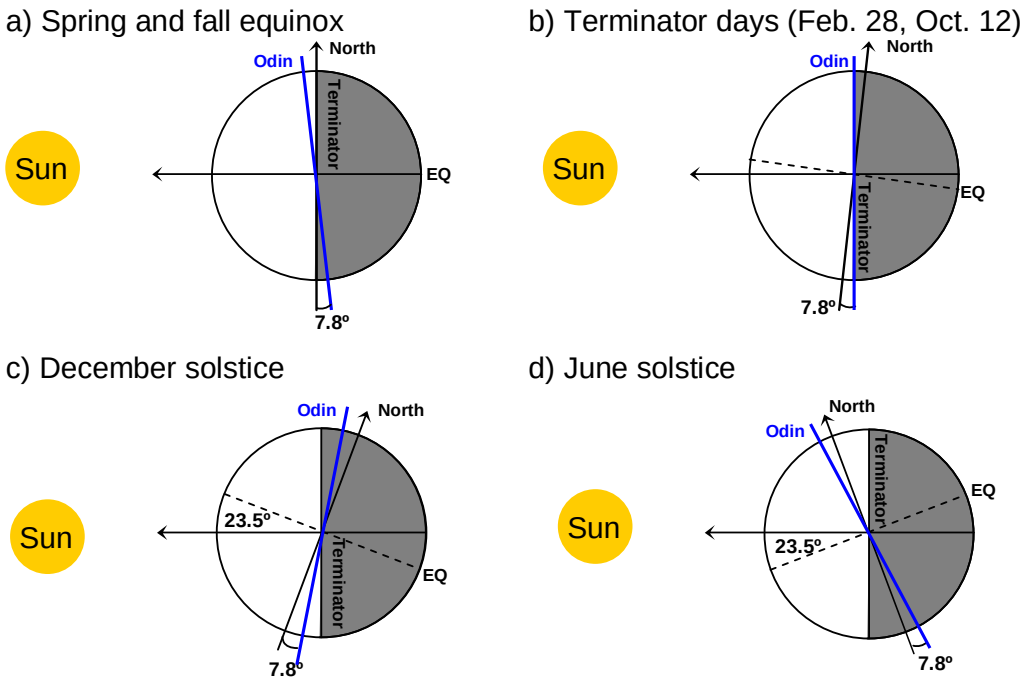

Figure 2.6: Precession of the Odin orbit throughout one year.

and the Submillimetre and Millimetre Radiometer (SMR). The SMR provides data for both astronomy and aeronomy objectives, while OSIRIS is exclusively dedicated to aeronomy experiments.

2.7 OSIRIS - The Optical Spectrograph and InfraRed Imaging System

The Optical Spectrograph and InfraRed Imaging System (OSIRIS) is the Canadian designed and built instrument on board Odin. When Odin makes measurements in astronomy mode with the SMR, OSIRIS is turned off. In aeronomy mode, the Optical Spectrograph scans the limb and makes approximately fifty spectrum measurements throughout the course of a single up- or down-scan. However, the InfraRed Imaging System (IRIS) continuously makes vertical limb measurements. OSIRIS and the SMR both look directly forward at the limb along the satellite track, although off-track observations are possible.

The OSIRIS limb-viewing measurement geometry is shown to scale in Figure 2.7. The bottom 100 km of atmosphere, the height range defined by the field of view of the IRIS, is represented in this figure by the blue annular ring. The position of Odin in orbit and the IRIS lines of sight for several positions along the satellite track are shown.

A wireframe diagram of the OSIRIS instrument is shown in Figure 2.8. The Optical Spectrograph is on the right side of the figure, and the three channels of the InfraRed Imaging system are on the left.

2.7.1 The Optical Spectrograph

The OSIRIS optical spectrograph (OS) is a grating spectrograph that covers the spectral range between 280 and 800 nm, with a resolution of approximately 1 nm. The OS is coaligned with the optical axis pixel of the IRIS, and as such provides the opportunity for intercalibration and comparison of the two instruments (Llewellyn *et al.*, 2004).

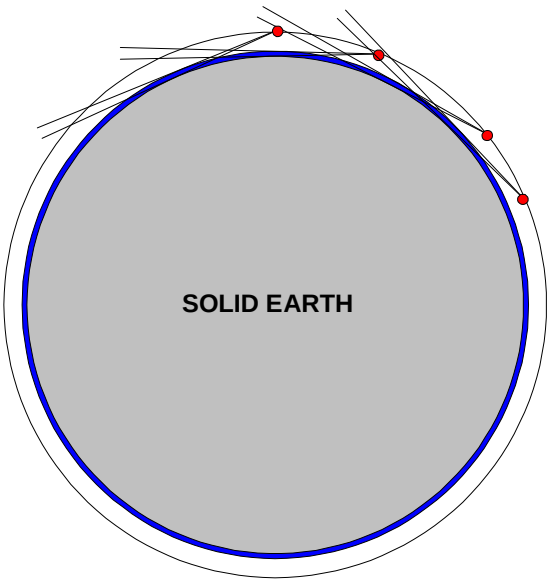

Figure 2.7: Scale representation of OSIRIS limb measurement geometry.

2.7.2 The Infrared Imaging System

The InfraRed Imaging System (IRIS) consists of three single lens interference filter imagers. Two channels observe radiation from the $O_2(a^1\Delta_g - X^3\Sigma_g^-)$ transition; the central wavelengths are at 1.263 μm and 1.273 μm, with Gaussian passbands of 10.0 nm FWHM. A third channel measures the OH Meinel bands at 1.530 μm with a tophat (rectangular) passband of 40.0 nm FWHM. The optical assembly of each channel consists of a baffle system, a combined shutter and calibration source, an interference filter, a zinc selenide lens, and a 128-element InGaAs linear array. The last 18 pixels of each linear detector array are masked for calibration purposes; the vertical field of view of each channel is approximately 100 km in the limb.

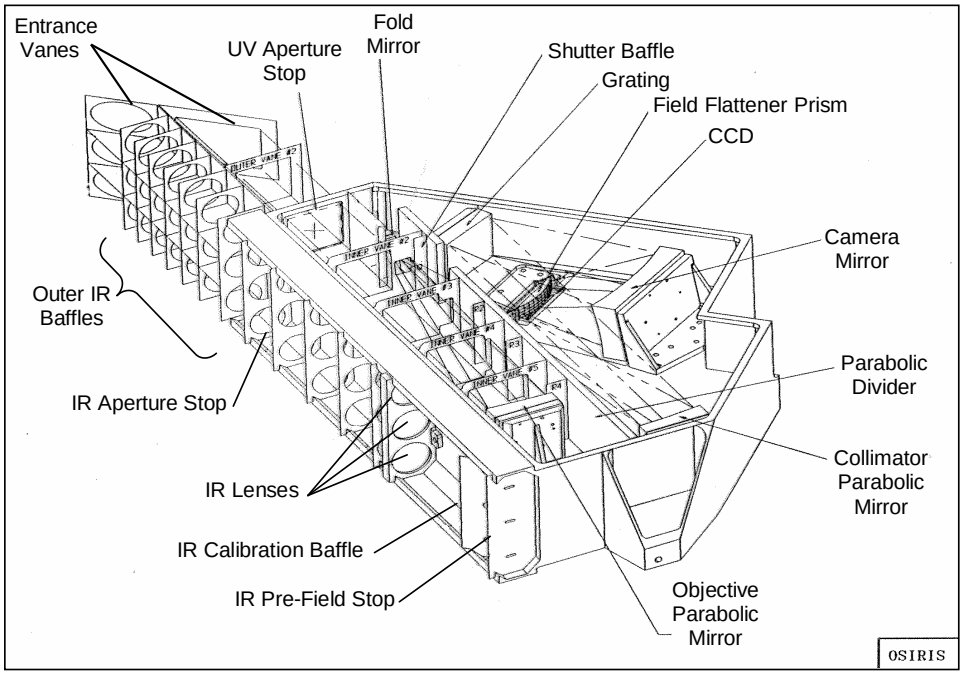

Figure 2.8: Wireframe diagram of the OSIRIS instrument.

2.8 $O_2(a^1\Delta_g)$ Measurements with the InfraRed Imaging System

A surface of the atmosphere 1 km in height and 2 km wide at the tangent point in the limb is imaged on to each pixel of the IRIS photodetector arrays. The photodetector arrays thus provide three simultaneous limb profiles of the measured brightness within their respective spectral regions. The limb brightness observations of the 1.27 μm emission are used as inputs to a tomographic technique that retrieves the volume emission profiles of $O_2(a^1\Delta_g)$. In this technique the line of sight intensity measurements from a large number of limb profiles are combined, with the result that a high-spatial resolution grid of volume emission rates along the satellite track is obtained.

The tomographic retrieval was developed from a technique used by Lloyd and

Llewellyn (1989) to deconvolve blurred images from a Fabry-Perot interferometer. The technique, which depends on photon counting statistics, was developed to solve the problem of recovering the radial profile of a spectral line from an off-center, distorted one-dimensional cross section of the interferometer pattern. The method finds the most likely distribution of photon counts that will account for the observations. In their study Lloyd and Llewellyn also considered the application of the technique to the recovery of volume emission profiles from rocket photometry experiments. McDade and Llewellyn (1991) extended this 'maximum probability' technique to the recovery of the two-dimensional distribution of auroral emission rates from tomographic rocket photometer measurements. The many measurements made throughout the rocket flight constitute a series of line integral measurements through the two-dimensional emission field that is to be retrieved. This idea was extended by Degenstein *et al.* (2003) to the problem of retrieving horizontal and vertical structure from a series of limb images taken aboard a satellite. This procedure was shown to accurately recover horizontal structure, on the order of 1° along the satellite track, even in the presence of significant random noise. This is the method that is applied to the IRIS limb observations to produce $O_2(a^1\Delta_g - X^3\Sigma_g^-)$ volume emission rate profiles along the satellite track.

The average data from several orbits of retrieved $O_2(a^1\Delta_g)$ concentrations obtained in this way are shown in Figure 2.9. In this figure the average of several orbits is used to capture the bulk features of the measurements; a single orbit of OSIRIS observations leads to very high-spatial resolution results that can mask the bulk features. The data obtained in a daily average, Figure 2.9, will be used for comparison purposes in Chapter 3.

The coordinates in this figure are: horizontally, the angle along the satellite track from the ascending node, and vertically, the geodetic altitude. The data shown are the average of eight orbits of measurements made on June 21, 2003; this positions the orbit such that Odin makes daytime measurements in the northern hemisphere and the southern hemisphere is under nighttime conditions. Several regions due to the

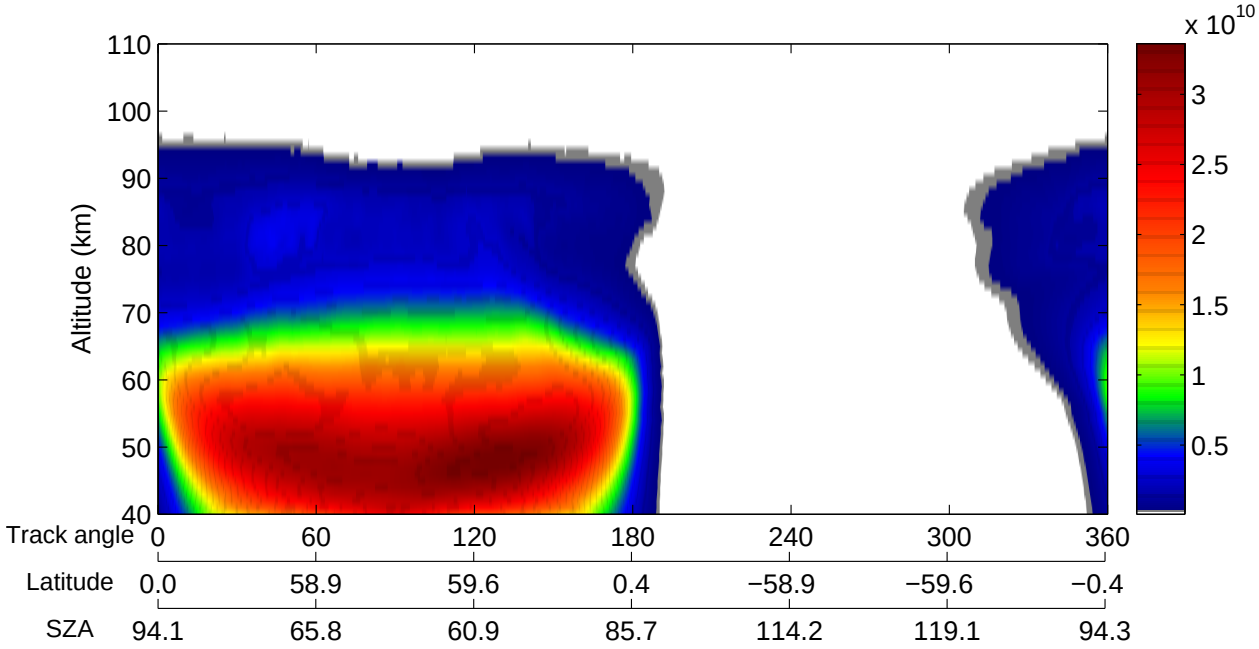

Figure 2.9: Average retrieved $O_2(a^1\Delta_g)$ concentrations [cm^{-3}] for eight orbits on June 21, 2003.

local time at the measurement point are apparent in this figure. Along the satellite track, the local time varies from local sunset at 0°, to local noon (90°), local sunrise (180°), local midnight (270°), and returns to local sunset at 360° along the satellite track. The large concentrations of $O_2(a^1\Delta_g)$ in the first half of the orbit are due to ozone photolysis in the illuminated portion, with a peak in the number density occurring near 50-55 km. The sunset and sunrise transition portions are clearly seen; the differences between the two are readily apparent. Sunrise shows a quick onset of photodissociation, whereas a long, slow decay is seen in the twilight on the sunset side of the orbit. The southern hemisphere section of the orbit is in darkness, and as such displays no photochemically produced $O_2(a^1\Delta_g)$. The presence of a faint secondary layer near 85 km in the nighttime portion of the observations corresponds to production by three-body recombination near the atomic oxygen peak.

The daytime measurements made by OSIRIS allow the determination of the ozone concentration in the mesosphere. In the next chapter the photochemical model used for the calculation of $O_2(a^1\Delta_g)$ concentrations from ozone and the retrieval of O_3 from the measurements is described.

Chapter 3

Photochemical Model

3.1 Introduction

This chapter provides a description of the photochemical software model developed in this work that is used to perform retrievals of ozone from measurements made by the OSIRIS InfraRed Imaging System channels. The most general form of the model is a one-dimensional, time-dependent photochemical model that takes as input a height profile of ozone concentrations and calculates the concentration height profile of $O_2(a^1\Delta_g)$. The components of the model and some results are presented in this chapter.

3.2 Photochemical Modeling

3.2.1 Continuity Equation

Atmospheric modeling requires the simultaneous solution of the continuity equations for all chemical species of interest. To solve for the temporal and spatial dependence of the volume mixing ratio $[X]$ of a chemical species the continuity equation is used,

$$\frac{\partial[X]}{\partial t} + \nabla \cdot (X\mathbf{u}) = S_X, \tag{3.1}$$

where $\mathbf{u}$ is the velocity of air through the volume, and S_X is the chemical forcing within the volume. For steady-state chemical forcing, S_X is zero, and any change in the number density accumulation is matched by a change in the flow into the volume.

When an instrument simultaneously measures both winds and chemical concentrations velocity information can be inferred, and used in the solution of the continuity equation. As the OSIRIS instrument does not measure wind, only the species concentrations can be determined. For the assumption of no transport, $\mathbf{u} = \mathbf{0}$ in equation (3.1), the continuity equation is expressed in terms of chemical production (P_X) and loss (L_X) terms. This allows for a solution for the species mixing ratio X,

$$\frac{\partial[X]}{\partial t} = P_X - L_X[X]. \tag{3.2}$$

The solution of the coupled continuity equations in this form, for the species $O_2(a^1\Delta_g)$, $O_2(b^1\Sigma_g^+)$, and $O(^1D)$, allows the ozone concentration to be determined from measured $O_2(a^1\Delta_g)$ concentration. The background atmosphere (N_2, O_2, O, and H concentrations) and temperature profiles used are from the MSIS model (Hedin, 1991). It should be noted that parameterizations of transport from other models could be included into future developments of this model, which is beyond the scope of this work.

3.2.2 Photochemical Production Coefficients

The production terms, P_X, in equation (3.2) typically involve photochemical processes. Calculation of photochemical coefficients depends on the solar flux available at the measurement point and the cross-section of the absorbing molecule. The monochromatic form of this calculation, at wavenumber ν, is

$$J_X(\nu) = F(\nu) \cdot \sigma_X(\nu), \tag{3.3}$$

where $F(\nu)$ is the solar flux at wavenumber ν, in $\frac{photons}{cm^2 \cdot s}$, and $\sigma_X(\nu)$ is the absorption cross section of molecule X at wavenumber ν in $\frac{cm^2}{photon \cdot molecule}$. A wavelength-

dependent quantum yield is included in the spectral data used in this model. The photolysis coefficient J_X has units of $\frac{photodissociations}{s \cdot molecule}$. The characteristics of the molecular absorption cross-sections depend upon the transitions available to a ground state molecule. Dissociative transitions typically display a continuous energy dependence, with banded structures at energies below the dissociation limit. These bands correspond to vibrational and rotational transitions between the different electronic states. The higher-energy end of a dissociative absorption region typically has a smooth, continuum-like, structure that is related to the continuous range of energies accessible beyond the dissociation limit. The absorption cross sections used in the present model are described in Sections 3.3.1 and 3.3.2. The absorption cross section is a function of temperature in the band regions due to both the varying population of rotational states and the temperature dependence of the absorption linewidths.

In practical computations of photochemical production terms, the solar flux $F(h, \nu)$ at a modeled height h is calculated as

$$F(h, \nu) = F_\infty(\nu) \exp[-\tau(h, \nu)], \tag{3.4}$$

where $F_\infty(\nu)$ is the 'outside of atmosphere' solar flux. The optical depth $\tau(h, \nu)$ is the total wavelength-dependent absorption of solar flux by the atmosphere down to height h. The attenuation due to each absorbing species must be included in the computation of the optical depth. For an absorbing species i, the optical depth at a measurement height, h, is calculated by determining the total pathlength of species i through which the solar radiation passes,

$$\tau_i(h, \nu) = \int_h^{h_\infty} n_i(s) \sigma_i(s, \nu) ds, \tag{3.5}$$

where the integration extends to a 'top of atmosphere' height, h_∞. The temperature dependence of the absorption cross section is characterized as a height dependence for the assumption of a stratified atmosphere. Optical depths for each absorbing species i, at each wavenumber ν are summed for all absorbing species to give the

total optical depth,

$$\tau(h,\nu) = \sum_{i=1}^{N} \tau_i(h,\nu). \tag{3.6}$$

The modeling in this thesis focuses on processes that are active in the ultraviolet region of the spectrum, namely attenuation due to O_2 and O_3 absorption and through Rayleigh scattering.

The solar flux data used to calculate photolysis coefficients in the model are from the UARS SOLSTICE observations; these values are the average of measurements made for solar maximum (January 1-March 31, 1992) and solar minimum (January 1-March 29, 1995) conditions. A wavelength-dependent parameterization of the change in incident solar flux that is due to solar cycle variation is included in the model. In the Hartley band the change in solar flux due to solar cycle variation is typically one percent.

3.3 Transmission of UV Solar Flux

3.3.1 Ozone Absorption Cross Section

The Hartley band of ozone is the primary absorber of middle- to near-ultraviolet light in the atmosphere; this absorption is also responsible for the production of $O_2(a^1\Delta_g)$ through reaction (2.6). The ozone absorption cross section used in the model (De More *et al.*, 1997) is shown in Figure 3.1. The small temperature dependence that exists in the Huggins bands, between 275 and 350 nm, is also included in the figure. The Chappuis bands in the visible region of the solar spectrum are responsible for absorption near the stratospheric ozone maximum. The small cross-sections due to absorption in the near-infrared Wulf bands are omitted from this figure.

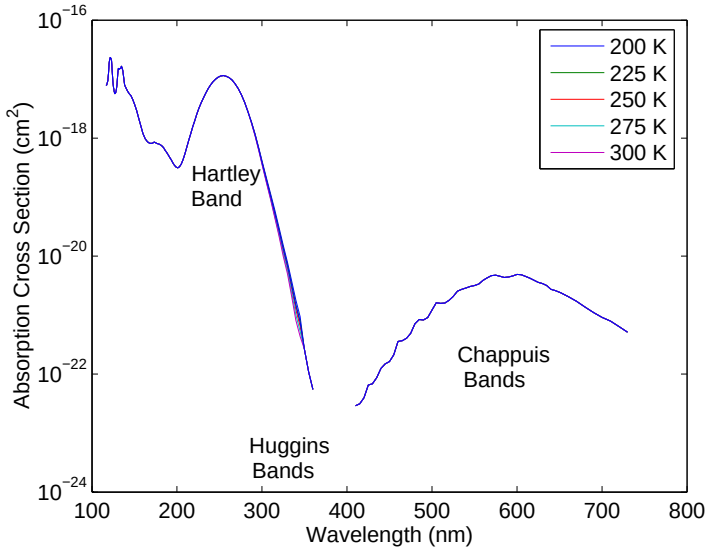

Figure 3.1: Absorption cross section of O_3.

3.3.2 Molecular Oxygen Absorption Cross Section

Absorption by molecular oxygen modifies the ultraviolet flux available for photolysis, and contributes to the production of $O_2(a^1\Delta_g)$ (reaction 2.11) through absorption in the Schumann-Runge continuum and by solar Lyman-α. The absorption cross section (De More *et al.*, 1997) for molecular oxygen is shown in Figure 3.2. The wavelength structure in the Schumann-Runge bands, which lie between 175 and 205 nm, is not shown. This highly structured absorption region corresponds to a predissociation,

$$O_2(B^3\Sigma_u^-) + h\nu(175 - 205 \text{ nm}) \longrightarrow O(^3P) + O(^3P), \tag{3.7}$$

that results from the crossing of a dissociative curve that can produce two ground state oxygen atoms. The extensive line structure in this region requires the absorption to be treated separately.

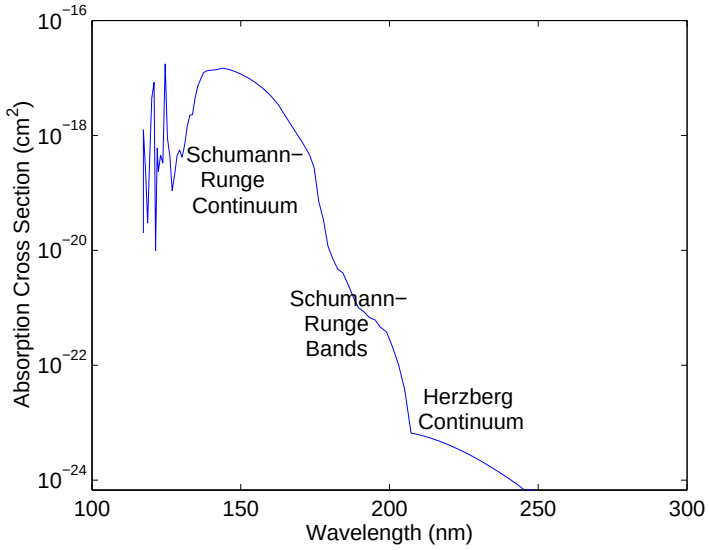

Figure 3.2: Absorption cross section of O_2.

3.3.3 Absorption in the Schumann-Runge Bands

The O_2 absorption cross section in the Schumann-Runge bands (SRB) at 300 K is shown in Figure 3.3. The onset of the Herzberg continuum is seen in this figure at 198 nm, where its absorption begins to exceed SRB absorption. An absorption parameterization developed by Kockarts (1994) is used in the present model. This parameterization divides the spectral range of the bands into 16 subregions; in each subregion the average optical depth over all wavenumbers in the subregion is adopted, and a functional fit of the average to the O_2 column is made. In each of the 16 subregions a functional fit to six decaying exponentials is performed. Twelve coefficients are fit for each region: the magnitude and scale factor for each exponential are determined by a nonlinear least squares technique that fits to the values obtained from a line-by-line, temperature-dependent calculation. This analysis results in two 'reduction factors' $R_j(O_2)$ and $R_j(M)$ being computed for each of the $j = 1 \ldots 16$ sub-regions. The reduction factors provide the transmission of the solar flux in the Schumann-Runge bands, and photolysis coefficients are computed for O_2

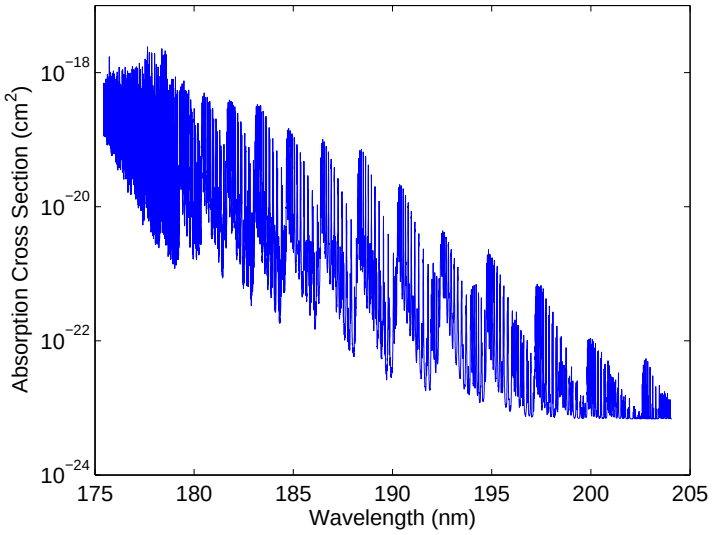

Figure 3.3: Absorption cross section of O_2 in the Schumann-Runge bands at 300 K.

as

$$J_{O_2}(\nu) = F(\nu)R_j(O_2)\exp\left[-(\tau_{Rayl}(\nu) + \tau_{O_3}(\nu))\right]. \tag{3.8}$$

Here the O_2 absorption cross section, $\sigma_{O_2}(\nu)$, is incorporated into the reduction factors $R_j(O_2)$. For all other species, X, in this region the photolysis coefficients are

$$J_X(\nu) = \sigma_X(\nu)F(\nu)R_j(M)\exp\left[-(\tau_{Rayl}(\nu) + \tau_{O_3}(\nu))\right]. \tag{3.9}$$

This wavelength region is important for calculation of the production of $O(^1D)$ through O_2 photolysis.

3.3.4 UV Solar Flux in the Mesosphere

The transmitted solar flux in the mesosphere can be calculated from the absorption cross sections for molecular oxygen, ozone, and an effective absorption cross section for Rayleigh scattering. The transmitted solar flux at several heights as calculated by the model, for a solar zenith angle of 70°, is shown in Figure 3.4. The three

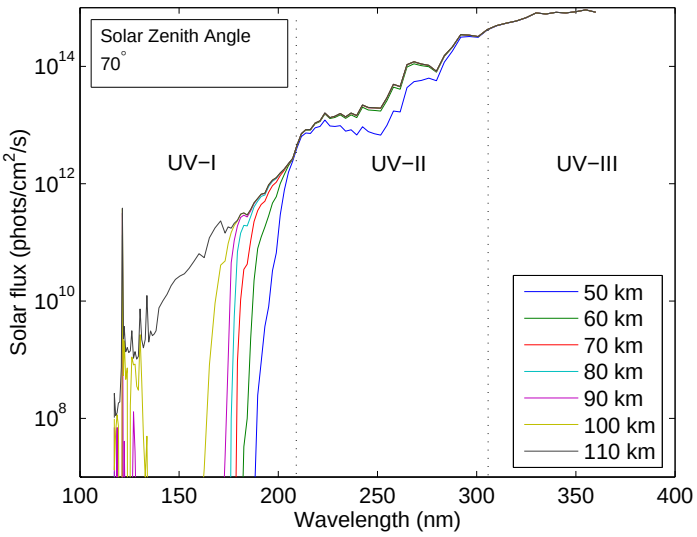

Figure 3.4: Transmitted solar flux in the mesosphere for a 70° solar zenith angle.

regions highlighted in this figure relate to the dominant absorbing species. Region UV-I, below 210 nm, is primarily absorbed by O_2 in the Schumann-Runge continuum and bands, and is significantly attenuated in the mesosphere. Absorption in region UV-II, between 210 and 310 nm, is primarily due to ozone absorption in the Hartley bands. Absorption in this region is very sensitive to the ozone column through which the solar radiation passes and increases significantly as the sun approaches the horizon. Attenuation in region UV-III, above 310 nm, is due to Rayleigh scattering. The attenuated solar flux for a solar zenith angle of 94° is shown in Figure 3.5. Here the sun is below the horizon and light passes through the stratospheric ozone maximum before the height of interest; thus the solar flux in the Hartley band is effectively cut off. This shadow effect cuts off production of $O_2(a^1\Delta_g)$; this is apparent in the twilight decay shown in Figure 2.9.

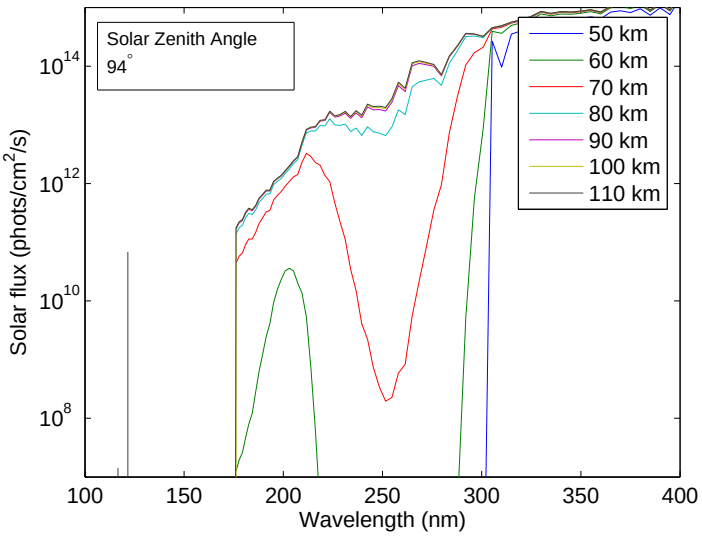

Figure 3.5: Transmitted solar flux in the mesosphere for a 94° solar zenith angle.

3.4 Photochemical Production Mechanisms

Photon absorption results in several possible fates for the absorber molecule that are dependant on the photon energy. Two cases are of particular interest for the present model. The first is photodissociation, in which a molecule is excited beyond the dissociation energy, and results in fragmentation; the second is photoexcitation, in this case the molecule is excited through absorption of a photon with the appropriate energy. The calculation of the rate coefficients for these processes is a key component in the model.

3.4.1 Photodissociation

Molecular photodissociation occurs when the internal energy of a molecule is raised above the dissociation limit and creates fragmentary products. The calculation of the photolysis coefficient, at a single energy, is shown in equation (3.3). However, molecular absorption can occur over an extended spectral region so that the calcu-

lation of the photolysis coefficient for absorption into a continuum involves the sum of contributions from all photon energies,

$$J_X(h) = \int_{\nu_1}^{\nu_2} \sigma_X(\nu) F_\infty(\nu) \exp(-\tau(h,\nu)) d\nu. \tag{3.10}$$

The integration is between upper and lower wavenumbers, ν_1 and ν_2, that define the transition energies. As the column densities of the absorber species increase with decreasing altitude in the atmosphere, photolysis coefficients increase with height, and reach the zero-optical depth value, J_∞, at the top of the atmosphere. The characteristics of photolysis coefficients in the mesosphere are illustrated in Figure 3.6, which shows the Hartley band photolysis coefficient calculated by the model for several solar zenith angles. The photolysis coefficients are seen to decrease from

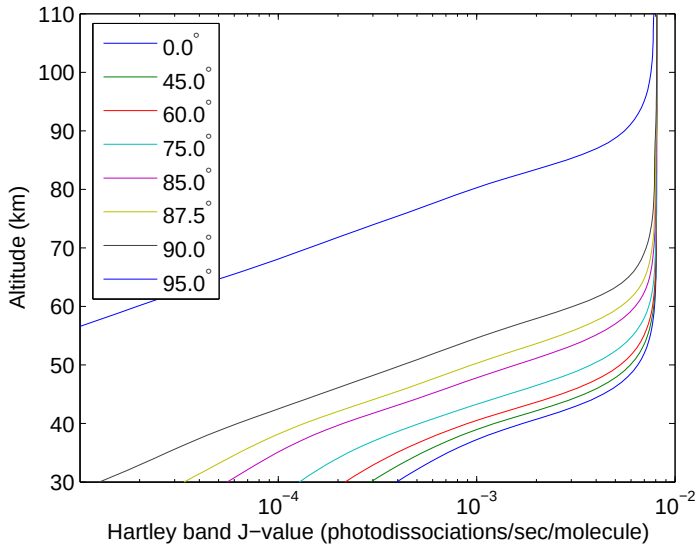

Figure 3.6: Height profile of Hartley band photolysis coefficient, as a function of solar zenith angle.

the zero optical depth value, J_∞, at different rates; this is due to the change in the absorber pathlength with solar zenith angle. The value J_∞ is a characteristic of the absorption cross section and the 'top of the atmosphere' solar flux, and has a value of 8.1×10^{-3} $\frac{photodissociations}{s \cdot molecule}$ for Hartley photolysis.

3.4.2 Photoexcitation

A molecule can be promoted directly into an electronically excited state through the absorption of a photon at the transition energy. In the model, photoexcitation occurs in the oxygen A-band, where a strong absorption feature at 762 nm results in the production of $O_2(b^1\Sigma_g^+)$, and in the OIRA bands, where photons near 1.27 μm can directly excite $O_2(a^1\Delta_g)$.

The rate coefficients for these photoexcitation processes, the g-values, are calculated in the same way as the photodissociation coefficients, equation (3.10). However, in photoexcitation transitions can occur between combinations of different vibrational-rotational levels in the two electronic states so that the absorption cross sections are highly structured. These cross sections must be explicitly calculated to account for both the temperature and pressure dependence of the absorption.

In a vibrational-rotational transition, absorption and emission occur at the allowable wavenumbers $\nu_{0,j}$, with each line having an associated absorption probability, S_j, that is governed by the populations of the rotational levels at that temperature. The absorption occurs in a spread of energies about the central line energy due to temperature (Doppler) and pressure (Lorentz) broadening. The shape of each line j is given by the Voigt profile, a convolution of the Doppler and Lorentz profiles,

$$\phi_{j,V}(\nu) = \phi_{j,D}(\nu) * \phi_{j,L}(\nu). \tag{3.11}$$

The absorption cross section at wavenumber ν is given by the sum of contributions from each of the N broadened lines in the transition,

$$\sigma(\nu) = \sum_{j=1}^{N} S_j \cdot \phi_{j,V}(\nu - \nu_{0,j}). \tag{3.12}$$

For the spectroscopic calculations performed in this work to determine photochemical coefficients, the line positions, $\nu_{0,j}$, and line strengths, S_j, from the HITRAN spectroscopic database were used. Line-by-line calculations of the cross section involve the construction of a high-resolution wavenumber grid that covers all relevant

energies ν in the transition; at each point ν, the cross-section is the sum of the contributions from all lines in the transition. As a much higher-resolution solar spectrum is needed for line-by-line models than for the photolysis coefficient calculations that are performed over energy continua, the data used for line-by-line calculations are from Kurucz (1995), which gives the solar irradiance at 1 cm^{-1} resolution.

The g-values, the photoexcitation rate per molecule, calculated by the model for the O_2 A-band transition at several solar zenith angles are shown in Figure 3.7. There are similar features to those for the photodissociation coefficients, namely a

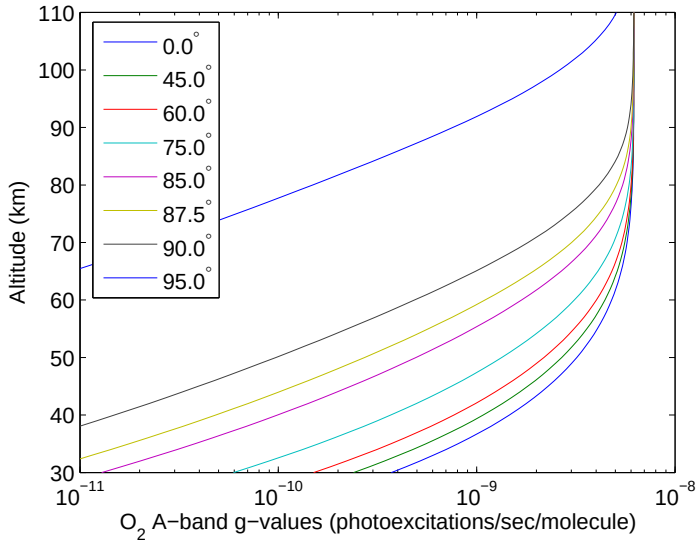

Figure 3.7: Height profile of A-band g-values, as a function of solar zenith angle.

decrease from the zero optical depth value and a decrease as the O_2 column increases. The zero optical depth value, g_∞, for the A-band calculated in the model is 6.1×10^{-9} $\frac{photoexcitations}{s \cdot molecule}$.

The line-by-line spectral calculations discussed in this section are computationally intensive, and cannot practically be determined with real-time processing. For this reason, two approaches have been taken to avoid direct calculations in modeling: g-values for solar conditions appropriate to the Odin orbit are pre-calculated,

and a parameterization of g-values as a function of O_2 column is made. The parameterization is discussed in Section 3.4.4.

3.4.3 Precalculation of g-values

The precalculated grids of photoexcitation coefficients are determined for the typical solar illumination throughout the Odin orbit. As the modeling is performed for every location along the orbit track, a sensible method of precalculation is to compute height profiles of g-values as a function of the angle along the satellite track; in this way the two-dimensional grid can be used as a lookup table. For the Odin geometry, zero degrees along the orbit corresponds to the equator crossing of the ascending node. As the orientation of the sun with respect to the Odin orbit varies throughout the year, these calculations must be made sufficiently often to represent accurately the illumination conditions in an orbit. For this reason the precalculations are made for each month using the solar conditions at the middle of each month.

The A-band g-values calculated by the model for the solar conditions during a June orbit are shown in Figure 3.8. The daytime and nighttime portions of the orbit are easily identified, as well as the twilight regions, in which the photoexcitation coefficient decreases upwards as the sun moves below the horizon.

3.4.4 Parameterization of Photochemical Coefficients

The parameterization of photochemical coefficients is done by fitting a functional form to a suitable set of independent variables. The data that are fit in this analysis are the production coefficients calculated from equation (3.10). The independent variables that determine the photoexcitation and photodissociation coefficients are the ozone and molecular oxygen column densities to the modeled point.

The attenuation of the solar flux near the $O_2(b^1\Sigma_g^+ - X^3\Sigma_g^-)$ and $O_2(a^1\Delta_g - X^3\Sigma_g^-)$ transitions due to O_3 absorption and Rayleigh extinction is negligible. For this reason a fit of the photoexcitation coefficients for both transitions to the O_2 column

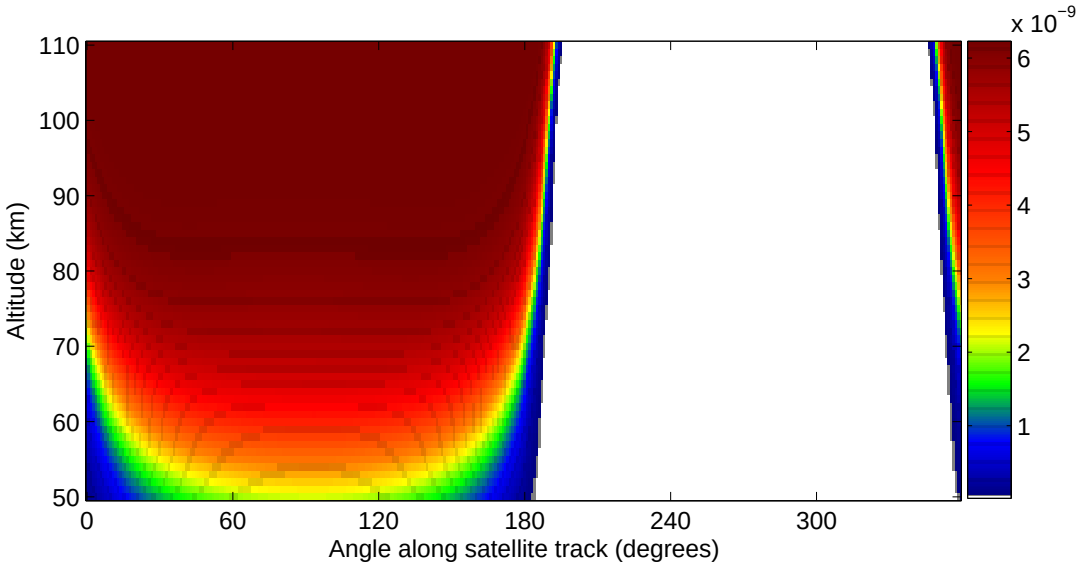

Figure 3.8: Calculated g-values $\left[\frac{photoexcitations}{molecule \cdot sec}\right]$ for a June orbit.

provides an appropriate parameterization. The g-values, calculated in this work by a line-by-line treatment, are shown for both transitions in Figure 3.9 as a function of O_2 column. The range of O_2 columns used in these parameterizations covers the full range encountered in mesospheric modeling; the largest column values shown correspond to a modeled height of 30 km at a solar zenith angle of 90°. Zhao and Turco (1997) found that the functional trend shown in Figure 3.9 can be fit by

$$g(N_{O_2}) = g_\infty \exp\left(-bN_{O_2}^c\right). \tag{3.13}$$

The fit coefficients b and c can be determined from a linear fit,

$$\ln\left(\ln\left(\frac{g_\infty}{g}\right)\right) = \ln(b) + c\ln(N_{O_2}), \tag{3.14}$$

when $\ln(\ln(\frac{g_\infty}{g}))$ is plotted as a function of $\ln(N_{O_2})$. A piecewise linear fit in this fashion allows for the parameterization of the g values as a function of O_2 column. The fitted results are shown in Figure 3.9 together with the line-by-line calculated data. The small amount of spread in the A-band g-values for O_2 columns between

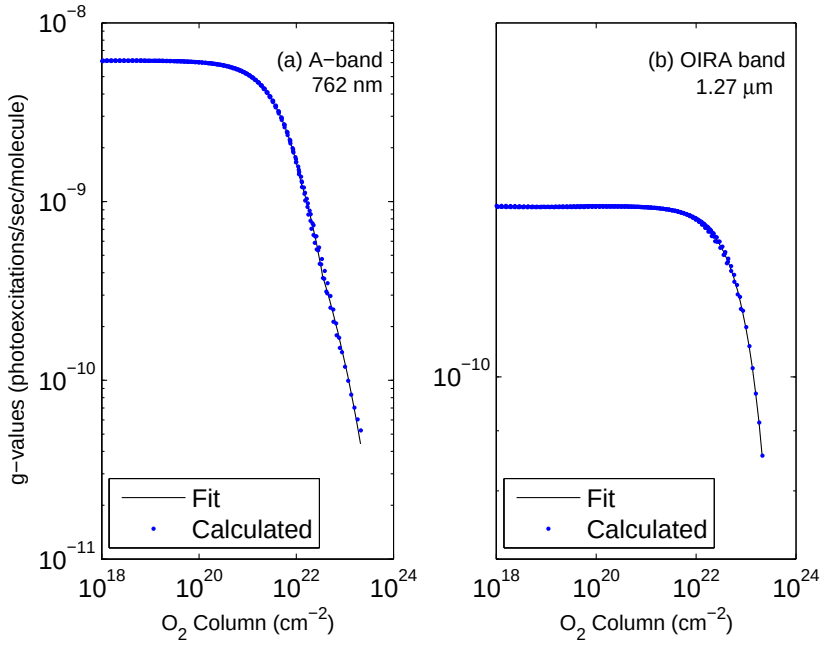

Figure 3.9: Fit of A-band and OIRA band g-values to O_2 column.

10^{22} and 10^{23} cm^2 is due to the temperature dependence of the lineshapes; this effect is omitted in the adopted parameterization. However, as the principal temperature and pressure variations in the atmosphere are associated with altitude, this variation can be treated by using the path-weighted absorption cross section,

$$\hat{\sigma}(\lambda, z) = \frac{\int_z^\infty \sigma[\lambda, T(z'), p(z')] n(z') dz'}{\int_z^\infty n(z') dz'}. \tag{3.15}$$

Zhao and Turco also showed that the g-value fit, Figure 3.9, is functionally equivalent to calculations that use the path-weighted absorption cross section. The typical mesospheric O_2 columns encountered range between 10^{18} and 10^{24} cm^{-2}. Within this range the functions provide an excellent fit. The data shown in Figure 3.9 can also be fitted with piecewise-continuous line segments corresponding to equation (3.12).

3.5 $O_2(a^1\Delta_g)$ Continuity equation

The photochemical reaction coefficients described in the previous section are the production terms in the continuity equations (3.2) that are solved in the model. For the production and loss mechanisms described in Section 2.4, the continuity equations are

$$\frac{d[O(^1D)]}{dt} = \Big(J_H[O_3] + \Big(J_{SRC} + J_{Ly-\alpha}\Big)[O_2]\Big) - \Big(A_D + k_D[Q_D]\Big)[O(^1D)], \quad (3.16)$$

$$\frac{d[O_2(b^1\Sigma)]}{dt} = \Big(g_\Sigma[O_2] + \phi k_{D,O_2}[O(^1D)][O_2]\Big) - \Big(A_\Sigma + k_\Sigma[Q_\Sigma]\Big)[O_2(b^1\Sigma)], \quad (3.17)$$

and

$$\frac{d[O_2(a^1\Delta)]}{dt} = \Big(J_H[O_3] + g_\Delta[O_2] + k_\Sigma[Q_\Sigma][O_2(b^1\Sigma)]\Big) - \Big(A_\Delta + k_\Delta[Q_\Delta]\Big)[O_2(a^1\Delta)]. \quad (3.18)$$

In these equations the photochemical production terms, J_H, J_{SRC}, $J_{Ly-\alpha}$, g_Σ, and g_Δ are all functions of time. The rate coefficients have the meanings shown in Figure 2.1. Coefficients J_{band}, g_X, $k_{X,q}$, and A_X represent photodissociation, photoexcitation, collisional quenching, and radiative decay respectively. The subscript convention refers to the effect on species X, and where photodissociation is over an energy band. It should be noted that a quantum efficiency ϕ limits the number of $O_2(b^1\Sigma_g^+)$ molecules produced from the collision of $O(^1D)$ with molecular oxygen. Unless otherwise noted, the rate coefficients used in this model are from the JPL chemical kinetics evaluation (Sander *et al.*, 2003).

The timescales for the coupled equations (3.16, 3.17, and 3.18) vary over several orders of magnitude. The characteristic times are ∼1 ms, 12 s, and ∼70 min, respectively. The solution of such a stiff set of equations, with time scales that differ by more than three orders of magnitude, is typically performed with a predictor-corrector variable-time step technique. A simpler alternative is to consider the short-lived species to be in a photochemical steady-state and to use their steady-state concentrations to calculate the time-dependent $O_2(a^1\Delta_g)$ concentration. It

follows that if $O(^1D)$ and $O_2(b^1\Sigma_g^+)$ are in steady state, then

$$[O(^1D)] = \frac{\eta J_H[O_3] + (J_{SRC} + J_{Ly-\alpha})[O_2]}{A_D + k_{q,D}[Q_D]} \tag{3.19}$$

and

$$[O_2(b^1\Sigma)] = \frac{g_\Sigma[O_2] + \phi k_{O_2,D}[O(^1D)][O_2]}{A_\Sigma + k_{q,\Sigma}[Q_b]}. \tag{3.20}$$

The substitution of these concentrations into equation (3.18) gives the time-dependent concentration of $O_2(a^1\Delta_g)$ as the solution of a single first-order differential equation. Time evolution of the $O_2(a^1\Delta_g)$ continuity equation is determined by calculating the photochemical coefficients at every time step and evolving the model forward from a known steady-state initial condition, namely local noon, to the measurement time.

$O_2(a^1\Delta_g)$ approaches a photochemical steady-state when OSIRIS measures within several months of summer solstice at high latitudes, where observations are made near local noon. In this region, the solar zenith angle is essentially constant during the measurement period so that the change in $O_2(a^1\Delta_g)$ concentration over the measurement period is very small. Thus it can be assumed that the $O_2(a^1\Delta_g)$ concentrations do not vary during the measurement period. In this region the continuity equation (3.18) can be solved in the steady-state form,

$$[O_2(a^1\Delta)] = \frac{\eta J_H[O_3] + g_\Delta[O_2] + k_{q,\Sigma}[Q_b][O_2(b^1\Sigma)]}{A_\Delta + k_{q,\Delta}[Q_a]}. \tag{3.21}$$

Equations (3.18) and (3.21) express the non-steady state and steady-state concentrations, respectively, of $O_2(a^1\Delta_g)$. In Chapter 4 the possibility of performing retrievals in both regimes is considered. However, for operational processing of the entire mission of OSIRIS data, only the steady-state form of the continuity equation, equation (3.21), is used. An analysis of the locations in the Odin orbit in which the steady-state approximation is valid is given in Section 4.2.

3.6 Modeled $O_2(a^1\Delta_g)$

The photochemical model can be run for a variety of situations, both in terms of the observing location and for different solar conditions. In this section, the results from several test cases of the photochemical model are presented.

3.6.1 Relative Contributions to $O_2(a^1\Delta_g)$

It is useful, when viewing height profiles of $O_2(a^1\Delta_g)$, to know the contributions from the various production mechanisms throughout the range of heights measured by the InfraRed Imaging System. Photochemical sources of $O_2(a^1\Delta_g)$ depend strongly on the solar zenith angle, and the modeled $O_2(a^1\Delta_g)$ in regions where these mechanisms dominate will also respond to any change in solar zenith angle. The amounts of $O_2(a^1\Delta_g)$ attributable to each of the production mechanisms discussed in Section 2.4, as calculated by the model developed in this work, are shown in Figure 3.10 for a solar zenith angle of 60°. It is apparent from this figure that the primary source

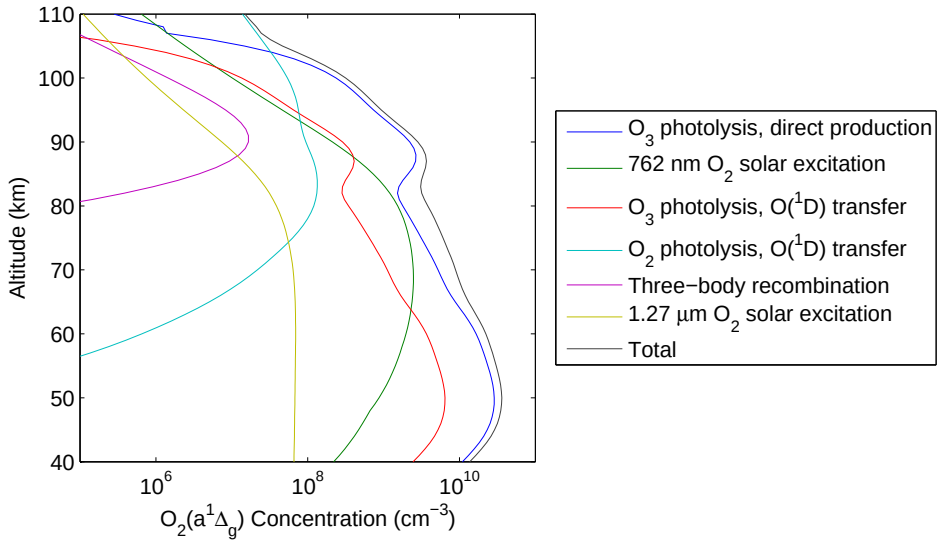

Figure 3.10: Amounts of $O_2(a^1\Delta_g)$ attributable to each production mechanism.

for $O_2(a^1\Delta_g)$ is direct production by O_3 photolysis. There is a secondary, parallel contribution from the co-product $O(^1D)$ through energy transfer (Q_2, Q_3). The photoexcitation-induced contribution from $O_2(b^1\Sigma_g^+)$ becomes a dominant source between 65 and 85 km. The contribution from Schumann-Runge continuum and Lyman-α O_2 photolysis is a dominant source above 90 km, but becomes negligible below 80 km. The production from three-body recombination, reaction (2.12), is visible near the atomic oxygen layer peak around 90 km. Similar analysis of the magnitude of contributions from each of the production mechanisms was performed by Mlynczak *et al.* (1993), and the results obtained in the current work agree well with their results.

3.6.2 $O_2(a^1\Delta_g)$ Variation with Solar Zenith Angle

A change in the solar zenith angle changes the pathlength of the solar radiation through the absorber species, which in turn causes a change in the photolysis coefficients. As the column through the absorbing species increases, so the photolysis rate decreases. The impacts of this effect can be understood through the following discussion. The $O_2(a^1\Delta_g)$ height profiles calculated with the photochemical model at a latitude of 52°N for a series of times, beginning after local noon and running through to twilight conditions, are shown in Figure 3.11. Several features are apparent in this figure. The number density peak rises as the sun nears the horizon and the solar radiation passes through a longer O_3 column. This results in large optical depths and in decreased production by O_3 photolysis. For solar zenith angles greater than ∼80°, there is significant quenching-related decay of $O_2(a^1\Delta_g)$ at lower altitudes, and O_3 photolysis ceases to produce $O_2(a^1\Delta_g)$. The decay is greatest at heights below 75 km, where the probability of quenching determines the lifetime of $O_2(a^1\Delta_g)$. Above this height, a $O_2(a^1\Delta_g)$ molecule has a greater probability of radiating than of quenching, and the solar zenith distance has a smaller effect on the $O_2(a^1\Delta_g)$ concentration. For heights between 80 km and 100 km production by

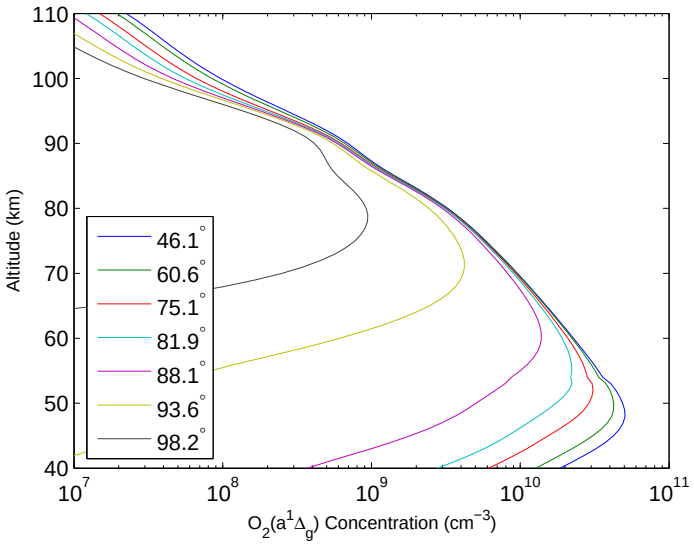

Figure 3.11: Height profile of $O_2(a^1\Delta_g)$ concentration, as a function of solar zenith angle.

three-body atomic oxygen recombination is significant. Above 90 km, production of $O(^1D)$ from Schumann-Runge dissociation of O_2 is the dominant source, and this production steadily decreases as the sun sets.

The diurnal variation of $O_2(a^1\Delta_g)$ at a given location can be found by integrating the continuity equation (3.18) over one day. The modeled $O_2(a^1\Delta_g)$ concentration for June 21, 2004 at Saskatoon, Saskatchewan (52°N) is shown in Figure 3.12. The features expected from the photochemistry are seen in this picture, notably a quick onset of photolysis in the morning as the sun rises, a relatively stable concentration throughout the day, and a slow decay of $O_2(a^1\Delta_g)$ at sunset, with the longest decay times occurring at high altitudes.

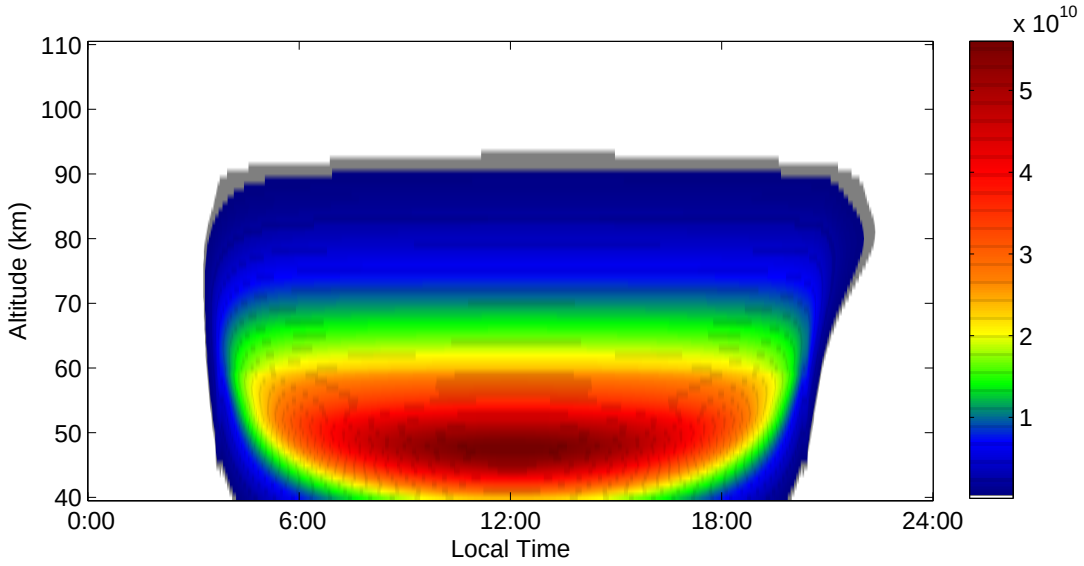

Figure 3.12: Modeled concentration [cm^{-3}] of mesospheric $O_2(a^1\Delta_g)$ at Saskatoon (52°N, 107°W) on June 21, 2004, from local midnight to local midnight.

3.7 Comparison of Modeled and Measured $O_2(a^1\Delta_g)$

The goal of the photochemical model developed in this work is to capture accurately the primary features of the structures seen by OSIRIS throughout the course of one orbit. Modeling is performed through a point-by-point run of the photochemical model; this involves integrating equation (3.18) for the $O_2(a^1\Delta_g)$ height profile at every point along the satellite track. The assumed concentrations of O_3 used in the model are from the Labow climatology (McPeters *et al.*, 1997). The climatology provides volume mixing ratios of ozone in 10° latitude bins for each month at heights up to 60 km. Above that height the climatological O_3 concentration is exponentially scaled with a scale height of 4.5 km, which is two-thirds the scale height of the neutral atmosphere. The modeled $O_2(a^1\Delta_g)$ for an orbit on June 21, 2003 is shown in Figure 3.13. The retrieved $O_2(a^1\Delta_g)$, averaged over eight orbits on June 21, 2003, was shown at the end of the previous chapter, and is repeated in Figure 3.14 for

comparison. There is excellent agreement is seen between the modeled and mea-

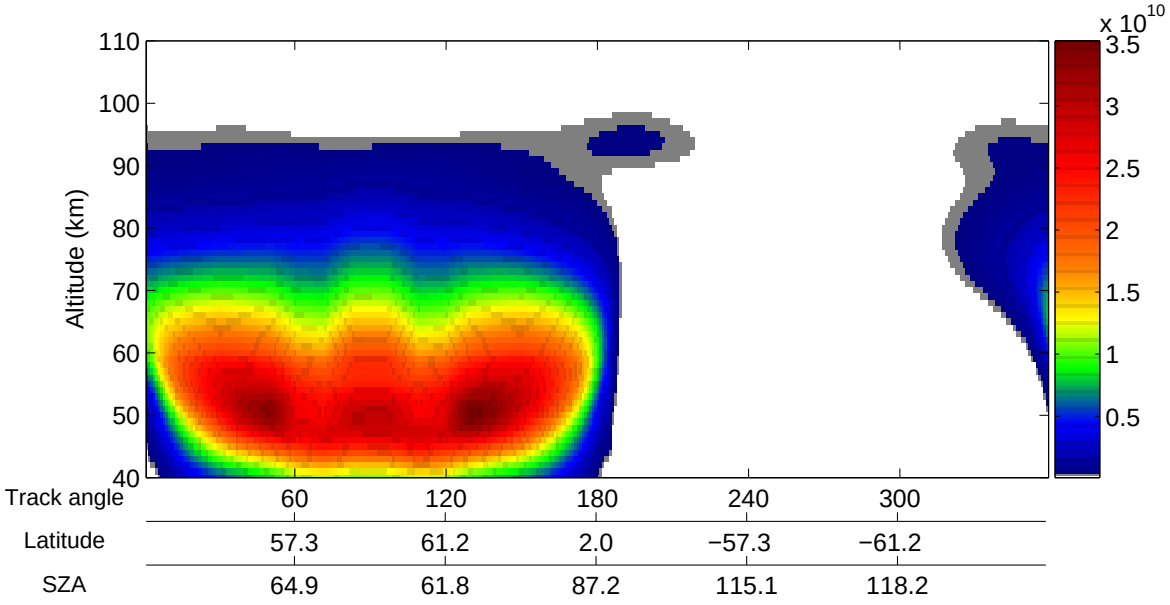

Figure 3.13: Modeled $O_2(a^1\Delta_g)$ concentrations [cm^{-3}] for a June 21, 2003 Odin orbit.

sured $O_2(a^1\Delta_g)$. However, one notable difference occurs at both 70 and 110° along the satellite track, where the modeled $O_2(a^1\Delta_g)$ concentration is lower at the peak value than the measurements. This discrepancy is due to lower O_3 concentrations within the 70° latitude bin in the climatology. Apart from this difference, there is a good agreement between the scale, photochemical features, and characteristic decay times at all points along the orbit track.

As the Odin orbit precesses throughout the year, the orientation of the orbit plane to the sun changes, and this in turn changes the photochemical conditions. The effect of this change can be seen in a comparison of the measured $O_2(a^1\Delta_g)$ seen in Figures 3.14 and 3.15. In the vernal equinox measurements, shown in Figure 3.15, the solar zenith angle changes much more gradually than during the summer solstice measurements. This is reflected by the sharp 'V' shape of the peak $O_2(a^1\Delta_g)$

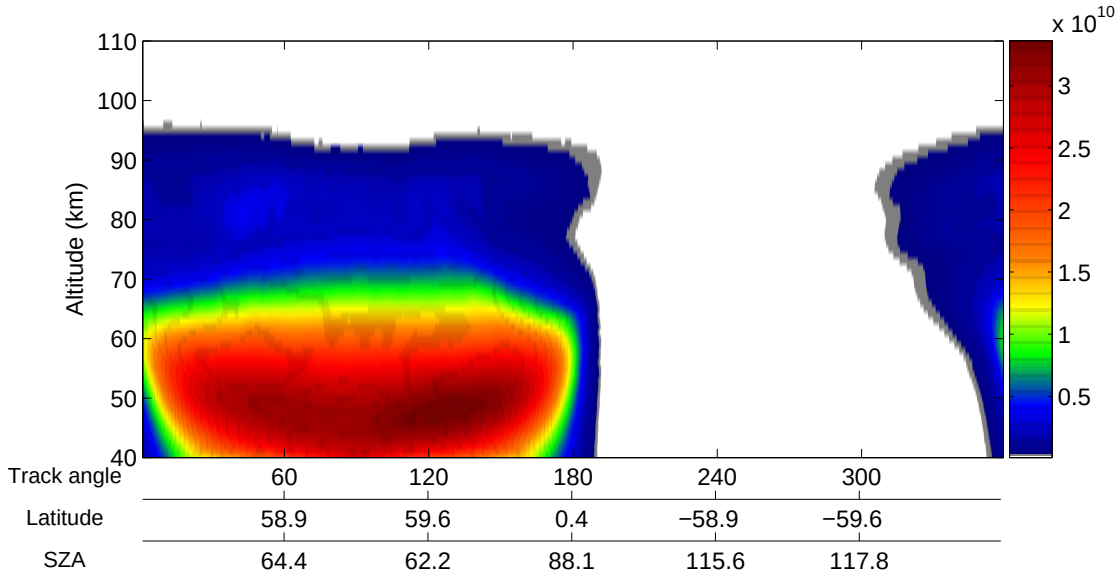

Figure 3.14: Retrieved $O_2(a^1\Delta_g)$ concentrations [cm^{-3}] for June 21, 2003.

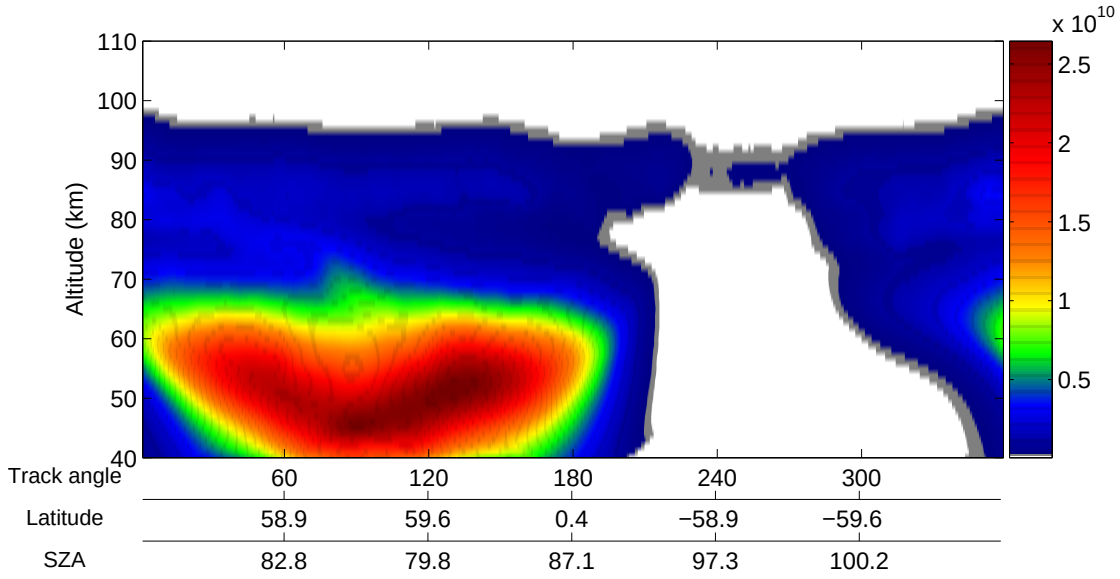

Figure 3.15: Retrieved $O_2(a^1\Delta_g)$ concentrations [cm^{-3}] for March 21, 2004.

concentration in the northern hemisphere. In addition the sunset and sunrise regions of the measurements at 0 and 180° along track, respectively, are more spatially extended in the March measurements. The modeled $O_2(a^1\Delta_g)$ concentrations for the vernal equinox orbit are shown in Figure 3.16. There is very good agreement

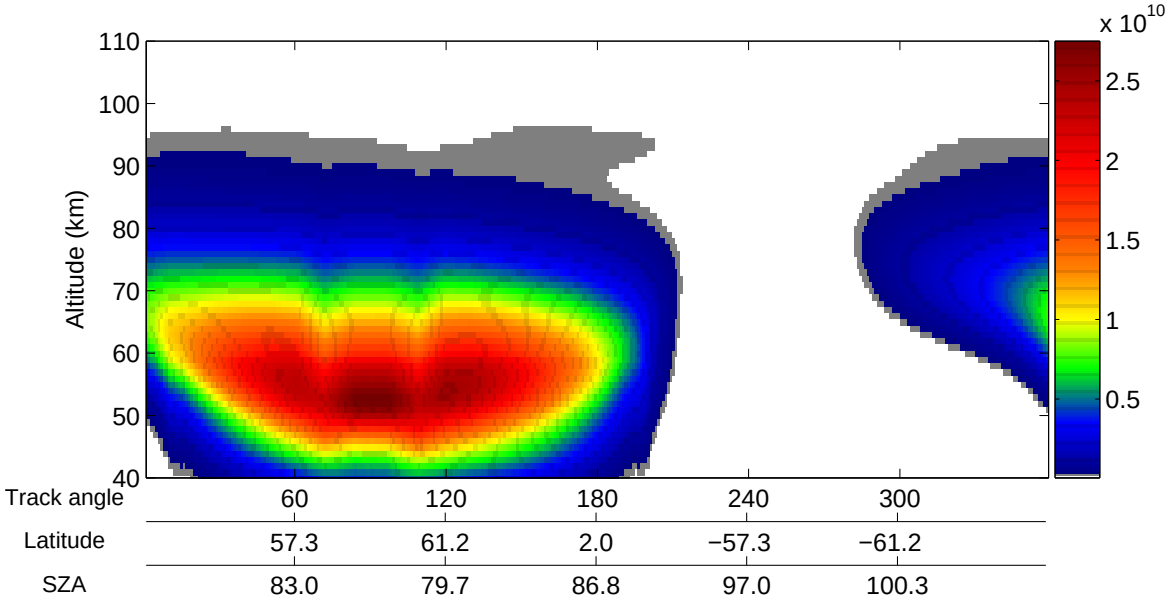

Figure 3.16: Modeled $O_2(a^1\Delta_g)$ concentrations [cm^{-3}] for a March 21, 2004 orbit.

between the modeled and measured results, and it is apparent that the model captures the varying photochemical conditions seen in the measurements. The lower concentrations present at 70 and 110° along track seen in the modeled June data are also present here, as the climatology in this region may not be properly representative of the O_3 concentration. There is a measured enhancement that is not seen in the modeled concentrations between 65 and 80 km and between 30 and 90° along track. This enhancement is a tertiary ozone maximum, and its chemistry has not been incorporated into the climatology. This feature is discussed in Section 5.4.

Comparisons between the vertical profiles of modeled and measured $O_2(a^1\Delta_g)$ at several points along the orbit track for a June 21, 2004 orbit are shown in Figure

3.17. It is apparent that there is good agreement between the modeled and measured

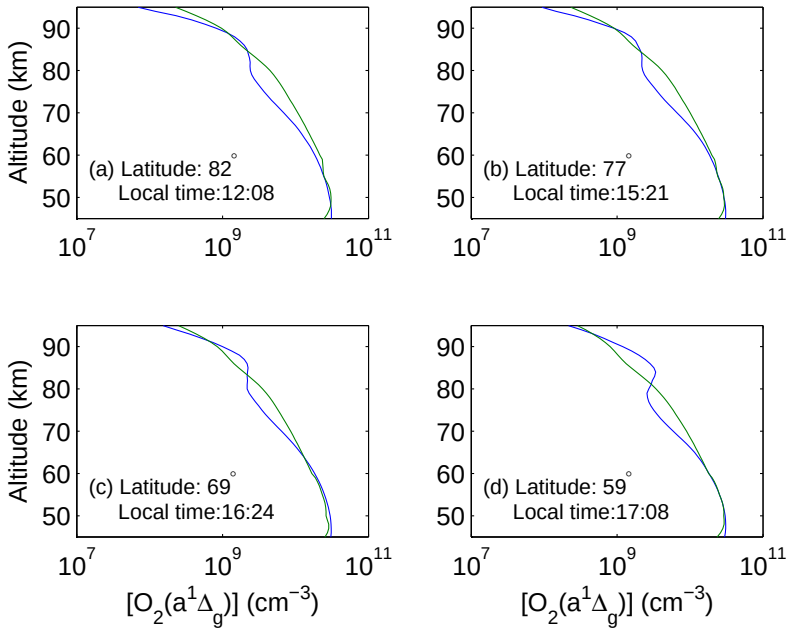

Figure 3.17: Comparison of measured (blue) and modeled (green) $O_2(a^1\Delta_g)$ concentrations: four points along the ascending node.

$O_2(a^1\Delta_g)$ between 45 and 70 km. Between 70 and 80 km, the modeled concentrations are systematically higher, and the model does not capture the secondary $O_2(a^1\Delta_g)$ concentration peak at 85 km. This is again a result of the climatological O_3 profile used in the modeling, which exponentially scales the O_3 concentration above 60 km and does not incorporate a secondary ozone peak near 85 km. It is shown in Chapter 5 that this does not present a problem for performing ozone retrievals, as the measured $O_2(a^1\Delta_g)$ structure near 85 km is correctly attributed as an ozone feature, and forward modeling with the retrieved results accurately captures the structure.

In the next chapter, the model is used in the retrieval of mesospheric ozone profiles. The validity of the assumption of photochemical steady-state is studied, and a review of retrieval techniques and a comparison of their suitability to the

problem are presented.

Chapter 4

Review of Retrieval Techniques

4.1 Introduction

With an appropriate forward model, it is possible to perform retrievals of key atmospheric quantities from relevant observations. The forward model described in the previous chapter is used to retrieve mesospheric O_3 for photochemical steady-state conditions in the Odin orbit. In this chapter those regions in which steady-state retrievals can be performed are described, and a comparison of several retrieval techniques is presented. The choice of retrieval technique depends on several factors, including suitability to the data, computational speed, and accuracy of the results. The retrieval techniques that have been tested in this study are:

1. A Levenberg-Marquardt nonlinear regression technique that performs iterations on the photochemical model to minimize the squared error between model results and measurements;

2. Optimal estimation, where a weighted average between the iterated O_3 and an *a priori* profile is taken;

3. An 'onion-peeling' algorithm that solves the photochemistry from the 'top of the atmosphere' to the bottom of the retrieval region; and

4. Steady-state and non-steady state nonlinear relaxation techniques.

The retrieval techniques are briefly described and compared. The performance of retrievals that employ both the non-steady state (equation 3.18) and steady-state (equation 3.21) continuity equations are examined in this chapter.

To simplify the notation in these discussions, the ozone height profile is expressed as a vector, $\mathbf{x}$, with elements x_i. The singlet delta height profile is expressed as a vector, $\mathbf{y}$, with elements y_j. The photochemical model described in the previous chapter serves as a function that relates the two vectors.

4.2 Steady-State Region Determination

If the photochemical steady-state equation (3.21) is used for retrievals, the steady-state configuration must be clarified and its regions of applicability throughout the Odin orbit defined. The magnitude of the time derivative $\frac{d[O_2(a^1\Delta_g)]}{dt}$ in the continuity equation (3.18) in relation to the concentration of $O_2(a^1\Delta_g)$ over the course of the Odin orbit can give an indication of where $O_2(a^1\Delta_g)$ is in steady state. It is expected that the daytime region of the orbit will be in photochemical steady-state and the ascending and descending node regions, which correspond to sunset and sunrise respectively, will show the largest values of $\frac{d[O_2(a^1\Delta_g)]}{dt}$. The evaluation of the time derivatives of $O_2(a^1\Delta_g)$ from the measurements and their use to determine steady-state conditions are described below.

4.2.1 In-Orbit Time Derivatives

The orientation of the Odin orbit with the ascending node at local sunset and the descending node at local sunrise, as shown in Figure 4.1, allows the calculation of the time derivative $\frac{d[O_2(a^1\Delta_g)]}{dt}$ from the retrieved $O_2(a^1\Delta_g)$ concentrations along the satellite track. As the suborbital point of Odin continually moves into earlier local times, the changing local time at the measurement points can be used to evaluate a

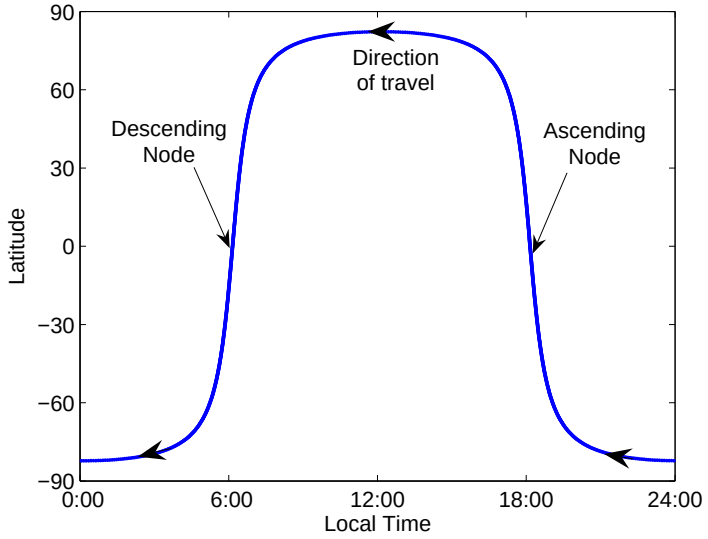

Figure 4.1: Odin latitude as a function of local time.

time derivative. The value $\frac{d[O_2(a^1\Delta_g)]}{dt}$ can be readily calculated with respect to local time through a central-difference technique at each point along the satellite track. This approach assumes that there are no differences due to latitudinal effects between the points used in the central difference. As there is no assumption of transport in the model, rigid rotation of the atmosphere with the earth is also assumed, and no advection terms enter the time derivative,

$$\frac{d[O_2(a)]_{(t)}}{dt} \simeq \frac{\Delta[O_2(a)]_{(t)}}{\Delta t} = \frac{[O_2(a)]_{(t+\Delta t)} - [O_2(a)]_{(t-\Delta t)}}{2\Delta t}, \tag{4.1}$$

where Δt is the change in local time between points along the satellite track. The time derivatives calculated for an orbit on June 21, 2003 are shown in Figure 4.2.

The effects of the $O_2(a^1\Delta_g)$ photochemistry are readily apparent in the calculated time derivatives. At points along the ascending node, local sunset, it is seen that the time derivative is large and negative from 40 to 70 km. This is due to the setting of the sun in these locations and the cessation of O_3 photolysis. On the descending node, at local sunrise, the time derivative is large and positive, corresponding

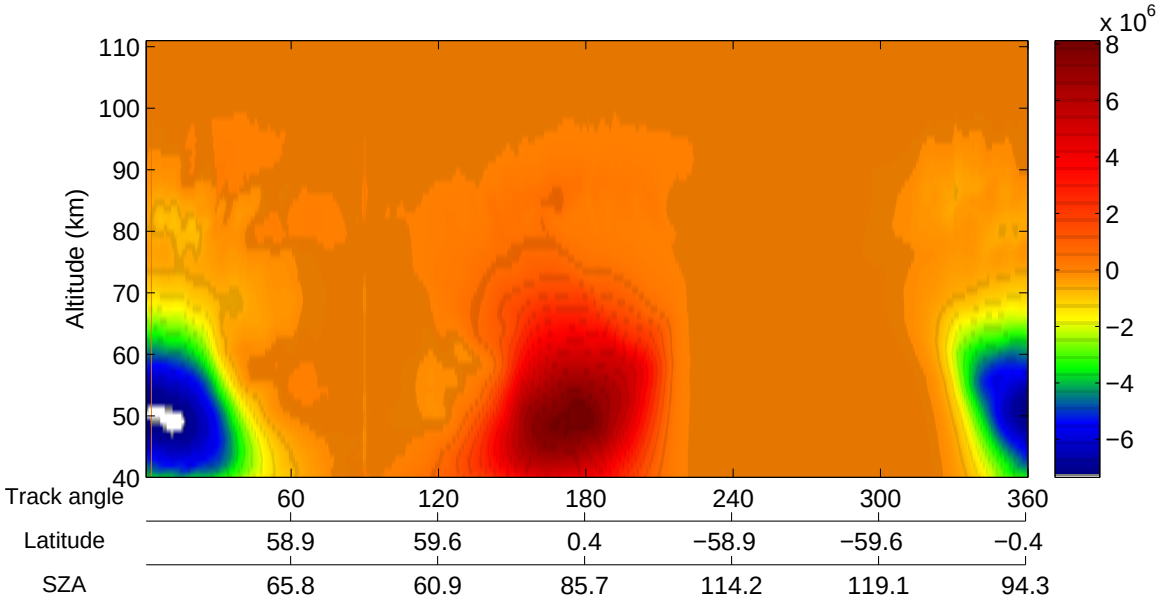

Figure 4.2: Calculated derivative $\frac{d[O_2(a^1\Delta_g)]}{dt}$ [$\mathrm{cm^{-3}s^{-1}}$] for an orbit on June 21, 2003.

to production by the onset of photolysis and resonant absorption. Photochemical steady-state conditions exist at altitudes above 75 km even when the sun is near the horizon, as the quenching lifetime becomes much less than the radiative lifetime, as was shown in Figure 2.2. The time derivatives calculated in this way provide a useful scale for the change in $O_2(a^1\Delta_g)$ at each measurement point. The structure seen above 80 km in the time derivatives is probably due to dynamical effects in the measurements that are not treated in the model.

4.2.2 Change in $O_2(a^1\Delta_g)$ over Measurement Time

The IRIS effectively samples a two-dimensional grid that consists of the lowest 100 km of atmosphere along the orbit track, as shown in Figure 2.7. This grid can be considered as a group of contiguous 'cells' that are arranged horizontally (0.2° spacing in angle along the satellite track) and vertically (1 km spacing). A

cell of the atmosphere defined in this way is measured by the IRIS by many lines of sight over an elapsed time. As Odin moves at 7 km/s in orbit and has a line of sight of 22° on a great circle, a single cell is sampled by OSIRIS for approximately five minutes. The change in $O_2(a^1\Delta_g)$ concentration over this time can be significant in the ascending and descending node regions. The fractional change in concentration over the measurement time can be determined using the time derivatives from equation (4.1) as

$$\%\text{Change}[O_2(a)] = \frac{d[O_2(a)]_{(t)}}{dt}\frac{\delta t}{[O_2(a)]_{(t)}}, \tag{4.2}$$

where δt is the elapsed measurement time and $[O_2(a)]_{(t)}$ is the concentration at the central measurement time.

The values of the percentage change in $O_2(a^1\Delta_g)$ concentration, calculated at six points along the orbit track beginning at the highest latitude (local noon) and moving down the ascending node towards the equator (sunset), for an orbit on June 21, 2003, are shown in Figure 4.3. This figure shows that there is no significant change in $O_2(a^1\Delta_g)$ concentration during the measurement time for latitudes above 30°. At lower latitudes, the lowest heights first begin to show non-steady state conditions, where the change over the measurement time becomes significant at a latitude of 15°. In Figure 4.3(e) and (f), it is seen that changes in concentration greater than 10% occur at heights below 50 km. It should be noted that the higher percentages seen above 75 km do not necessarily reflect photochemical-induced change. These heights are still illuminated throughout the ascending and descending nodes, and photolysis still occurs. However, as measurements at these heights tend to show significant structure due to dynamical effects that can change the concentrations of O_3 and atomic oxygen, these effects also appear in the calculated time derivatives. The steady-state region over the course of one orbit is indicated with the time derivatives $\frac{d[O_2(a^1\Delta_g)]}{dt}$ in Figure 4.4.

The effect of the change of season on the assumption of steady-state can be seen by looking at the percentage changes measured for an orbit near the spring

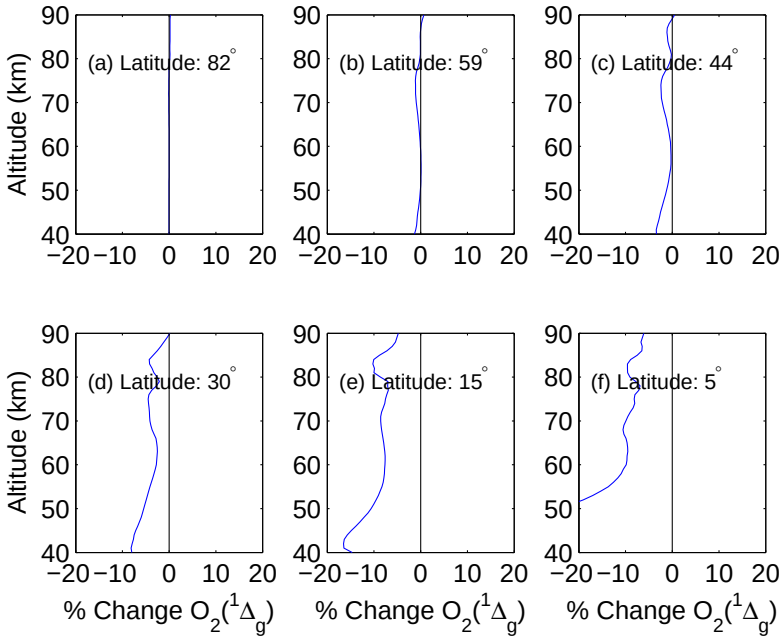

Figure 4.3: Percent change in $O_2(a^1\Delta_g)$ concentration: six points along the ascending node for an orbit on June 21, 2003.

equinox. Percentage changes for an orbit on March 18, 2004 are shown in Figure 4.5. The change in $O_2(a^1\Delta_g)$ concentration throughout the measurement period in these measurements is greater than for the June measurements by nearly a factor of two. Thus steady-state retrievals can only be used on a limited amount of the measurements away from the solstice conditions.

For our purposes, we define that for a change in concentration less than 5% over the measurement time, $O_2(a^1\Delta_g)$ can be considered to be in photochemical steady-state, and equation (3.21) can be used to perform ozone retrievals. This suggests that the retrieved ozone concentration may have a corresponding 5% uncertainty due to this change. This is the worst-case situation as the lowest altitudes are observed for a time shorter than 5 minutes.

Analysis was performed in this work to identify the photochemical steady-state

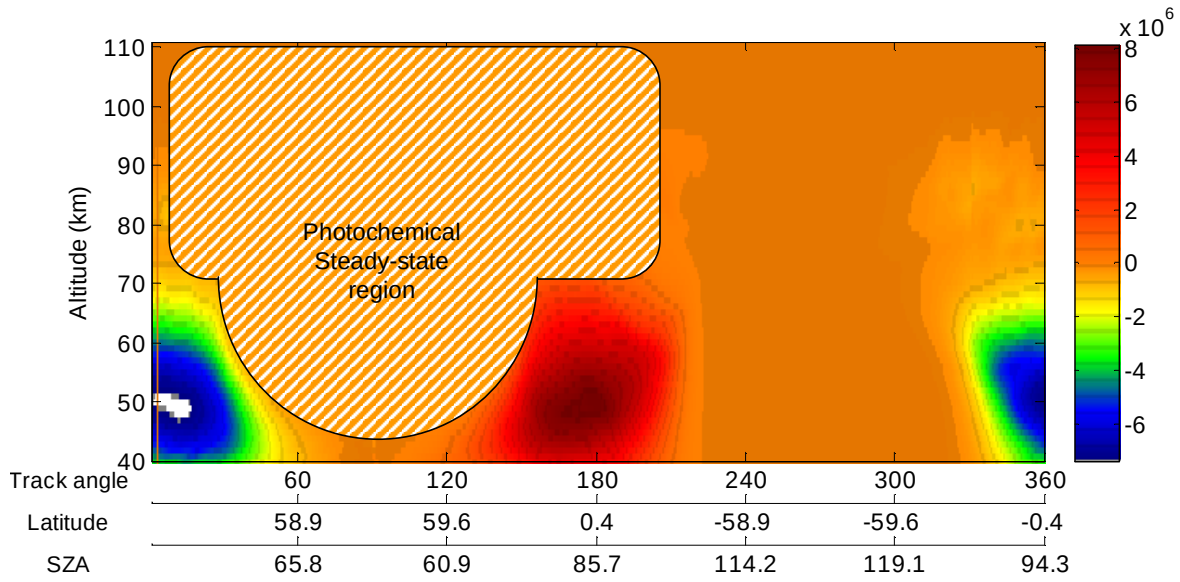

Figure 4.4: Calculated derivative $\frac{d[O_2(a^1\Delta_g)]}{dt}$ [$\mathrm{cm^{-3}s^{-1}}$] for an orbit on June 21, 2003.

regions of the orbit, as defined, on a monthly basis as a function of latitude. As the solar zenith angles along the ascending and descending nodes are generally different, the steady-state regions will not be symmetric in latitude along the ascending and descending nodes. The minimum heights of the regions in which steady-state conditions exist, for both ascending and descending node regions in 10° latitude bins, are shown for the northern hemisphere in Table 4.1 and for the southern hemisphere in Table 4.2.

The minimum heights of the photochemical steady-state region, as a function of latitude, are shown for May to August in Figure 4.6. It is seen in this figure that for months centered on summer solstice, photochemical steady-state conditions exist for all measured heights for latitudes above 45°. At lower latitudes, the minimum height of the steady-state region rises as the sun nears the horizon. The higher solar zenith angles during the descending node cause the asymmetry seen in this figure. The reversal of this trend during daytime measurements made in the southern hemisphere can be seen in Figure 4.7.

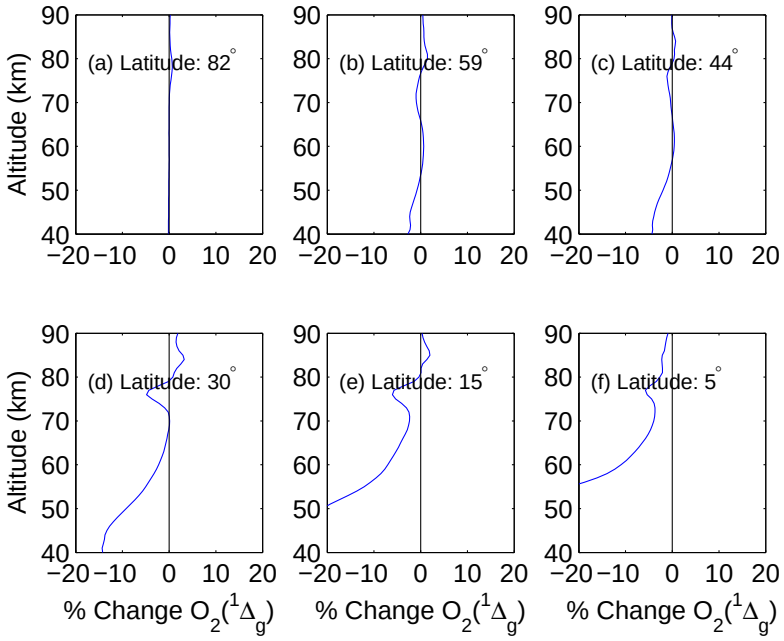

Figure 4.5: Percent change in $O_2(a^1\Delta_g)$ concentration: six points along the ascending node for an orbit on March 21, 2004.

With this assumption of photochemical steady-state conditions at the measurement point, the quantity that is retrieved is the mesospheric O_3 profile at local noon conditions at the measurement point.

4.3 Retrieval Techniques

A survey of retrieval techniques that have been implemented in this work with the photochemical model is presented. The first four techniques employ the steady-state form of the continuity equation (3.21) and the fifth employs the non-steady state form, equation (3.18).

Month	Center of Latitude Bin								
	5°N	15°N	25°N	35°N	45°N	55°N	65°N	75°N	85°N
March	$\frac{60}{75}$	$\frac{60}{70}$	$\frac{55}{60}$	$\frac{50}{50}$	$\frac{45}{45}$	$\frac{45}{45}$	$\frac{45}{45}$	$\frac{45}{45}$	$\frac{45}{45}$
April	$\frac{70}{75}$	$\frac{65}{55}$	$\frac{60}{50}$	$\frac{50}{45}$	$\frac{50}{45}$	$\frac{45}{45}$	$\frac{45}{45}$	$\frac{45}{45}$	$\frac{45}{45}$
May	$\frac{75}{75}$	$\frac{65}{55}$	$\frac{60}{45}$	$\frac{50}{45}$	$\frac{45}{45}$	$\frac{45}{45}$	$\frac{45}{45}$	$\frac{45}{45}$	$\frac{45}{45}$
June	$\frac{75}{75}$	$\frac{65}{55}$	$\frac{60}{45}$	$\frac{50}{45}$	$\frac{45}{45}$	$\frac{45}{45}$	$\frac{45}{45}$	$\frac{45}{45}$	$\frac{45}{45}$
July	$\frac{75}{75}$	$\frac{70}{60}$	$\frac{55}{45}$	$\frac{50}{45}$	$\frac{45}{45}$	$\frac{45}{45}$	$\frac{45}{45}$	$\frac{45}{45}$	$\frac{45}{45}$
August	$\frac{75}{75}$	$\frac{70}{60}$	$\frac{60}{50}$	$\frac{50}{45}$	$\frac{45}{45}$	$\frac{45}{45}$	$\frac{45}{45}$	$\frac{45}{45}$	$\frac{45}{45}$
September	$\frac{70}{75}$	$\frac{60}{65}$	$\frac{60}{45}$	$\frac{50}{45}$	$\frac{45}{45}$	$\frac{45}{45}$	$\frac{45}{45}$	$\frac{45}{45}$	$\frac{45}{45}$

Table 4.1: Minimum height (Ascending node/Descending node) in kilometers of steady-state regions by month: northern hemisphere.

Month	Center of Latitude Bin								
	5°S	15°S	25°S	35°S	45°S	55°S	65°S	75°S	85°S
October	$\frac{70}{70}$	$\frac{65}{50}$	$\frac{60}{45}$	$\frac{55}{45}$	$\frac{45}{45}$	$\frac{45}{45}$	$\frac{45}{45}$	$\frac{45}{45}$	$\frac{45}{45}$
November	$\frac{75}{55}$	$\frac{70}{50}$	$\frac{60}{45}$	$\frac{55}{45}$	$\frac{45}{45}$	$\frac{45}{45}$	$\frac{45}{45}$	$\frac{45}{45}$	$\frac{45}{45}$
December	$\frac{75}{70}$	$\frac{70}{60}$	$\frac{55}{50}$	$\frac{45}{45}$	$\frac{45}{45}$	$\frac{45}{45}$	$\frac{45}{45}$	$\frac{45}{45}$	$\frac{45}{45}$
January	$\frac{60}{75}$	$\frac{50}{75}$	$\frac{45}{75}$	$\frac{45}{55}$	$\frac{45}{45}$	$\frac{45}{45}$	$\frac{45}{45}$	$\frac{45}{45}$	$\frac{45}{45}$
February	$\frac{45}{75}$	$\frac{45}{75}$	$\frac{45}{75}$	$\frac{45}{75}$	$\frac{45}{65}$	$\frac{45}{45}$	$\frac{45}{45}$	$\frac{45}{45}$	$\frac{45}{45}$

Table 4.2: Minimum height (Ascending node/Descending node) in kilometers of steady-state regions by month: southern hemisphere.

4.3.1 Levenberg-Marquardt Nonlinear Regression

The retrieval of ozone concentrations from a set of $O_2(a^1\Delta_g)$ measurements can be approached as a nonlinear regression problem in which the ozone height profile is modified to minimize the squared error χ^2 between the modeled and measured $O_2(a^1\Delta_g)$. The problem is nonlinear because the calculated photolysis coefficient,

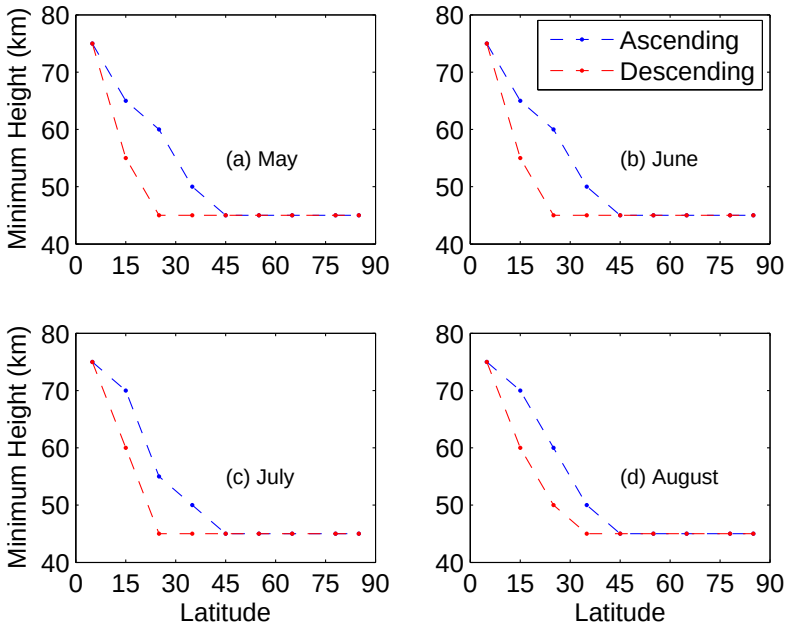

Figure 4.6: Latitude and minimum heights of photochemical steady-state region by month: northern hemisphere.

equation (3.10), depends exponentially on the ozone column above the measurement point. Because of this nonlinearity an iterative solution is used.

Levenberg-Marquardt regression (Press *et al.*, 1992) uses a combination of steepest-descent and inverse-Hessian error-minimization techniques. At each iteration, a weighting function matrix, $\mathbf{K}$,

$$K_{ij} = \frac{\partial y(j)}{\partial x(i)} \approx \frac{\Delta y(j)}{\Delta x(i)}, \tag{4.3}$$

is calculated. This corresponds to the change in each measured $O_2(a^1\Delta_g)$ concentration, $y(j)$, for a unit change in each O_3 concentration, $x(i)$. The weighting functions are evaluated by perturbing each O_3 concentration in the height profile by an amount, $\Delta x(i)$, and calculating the resulting change in the $O_2(a^1\Delta_g)$ concentration, $\Delta y(j)$. To approximate the derivative, a 0.25% perturbation is added to each of the O_3 concentrations.

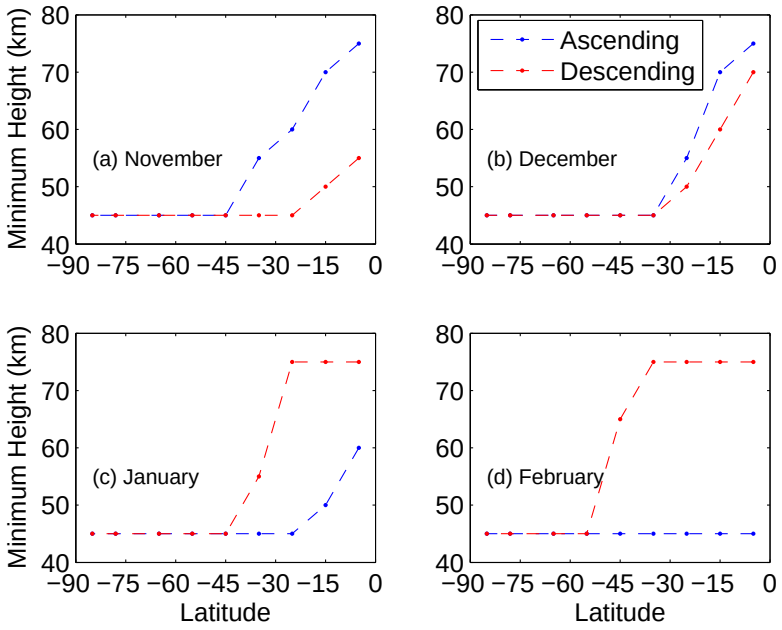

Figure 4.7: Latitude and minimum heights of photochemical steady-state region by month: southern hemisphere.

A matrix equation is solved to provide the update in the O_3 profile, $\Delta\mathbf{x}$, at the current step,

$$\mathbf{A} \cdot \Delta\mathbf{x} = \mathbf{b}. \tag{4.4}$$

Elements of the matrix A_{kl} contain values of the mixed second derivatives $\frac{\partial^2\chi^2}{\partial x_k \partial x_l}$ from cross-terms in the weighting function, and elements of $\mathbf{b}$ are the product of the modeled-measured difference with the first derivatives $\frac{\partial\chi^2}{\partial x_k}$. A selection parameter within the diagonal elements of the matrix $\mathbf{A}$ determines the choice of minimization technique used. When the error χ^2 is large, $\mathbf{A}$ becomes diagonally dominant, and a steepest-descent technique is used to calculate $\Delta\mathbf{x}$. As the solution approaches the minimum and χ^2 decreases, the diagonal elements no longer dominate, and the inverse-Hessian solution determines the next step in parameter space.

4.3.2 Optimal Estimation

Optimal estimation (Rodgers, 1976) is a standard retrieval technique employed in satellite remote sensing. Its goal is to estimate inputs to a model that are most consistent with the observations, given the measurement error. The technique finds an estimate of a quantity $\hat{x}$ using the weighted average of two independent measurements x_1 and x_2 with standard deviations σ_1 and σ_2,

$$\hat{x} = \left(\frac{1}{\sigma_1^2} + \frac{1}{\sigma_2^2}\right)^{-1}\left(\frac{x_1}{\sigma_1^2} + \frac{x_2}{\sigma_2^2}\right). \tag{4.5}$$

A priori information is assumed about the nature of the solution and is used as a 'virtual measurement' of the quantity to be retrieved. This gives the *a priori* the same status within the retrieval technique as the measurements. The two 'measurements' in equation (4.5) are the physical measurement and the *a priori* information, weighted by the inverses of their covariances and combined as an estimate to the solution. When equation (4.5) is expressed in matrix form, the standard deviations σ become covariance matrices that express the covariance between the ozone concentrations at different heights. The addition of the *a priori* constraint to the retrieval adds a 'smoothing' criterion to the retrieval, and ensures that the retrieved results will, on average, be evenly distributed about the *a priori* profile. In this work, the ozone concentrations from the Labow climatology are used as the *a priori* data. This technique has the advantage of wide acceptance in the remote sensing community and yields results that do not differ significantly from the expected results. However, the use of an *a priori* constraint will necessarily suppress results that are not in accordance with the assumed form of the solution.

The nonlinearity of the retrieval problem is handled in optimal estimation by using an iterative approach to the solution. At each iteration, a weighting function matrix (4.4) is calculated, and the step taken in parameter space is calculated according to the average of the *a priori* and the difference between the model and measurements. The inverses of the error in the measurements and modeled values are used to weight their contributions.

4.3.3 Onion-Peeling

The retrieval schemes discussed to this point use iterative approaches to the solution, successively approximating the solution by minimizing some error value. Both techniques require the calculation of a weighting function to determine the step to be taken in parameter space. For a retrieval that solves for M parameters, each weighting function calculation requires M forward model calculations, as the individual forward model responses to small perturbations in each input parameter is required. In addition, matrix inversions are required for both techniques. Such a computationally intensive retrieval scheme severely limits the ability to process a massive amount of data; there are on the order of ten thousand orbits of observations with the OSIRIS instrument already available.

However, it is possible to determine the O_3 concentrations without the calculating weighting functions. The 'onion-peeling' approach solves the continuity equation (3.21) for a series of heights in a top-down fashion. The zero-optical depth photolysis coefficient, J_∞, discussed in Section 3.4.1, is used at a 'top of the atmosphere' height to calculate the O_3 concentration through the continuity equation (3.18). This concentration is then incorporated into a calculation of the ozone column to a point below, where the O_3 photolysis coefficient is calculated at a lower height. This new J-value can then give the O_3 concentration at that height through the solution of the continuity equation at this lower height. By solving equation (3.18) sequentially downward to the bottom of the retrieval region, a height profile of mesospheric ozone is obtained.

This technique is conceptually simple, avoids the calculation of weighting functions, and easily provides O_3 concentrations from $O_2(a^1\Delta_g)$ measurements. However, this technique can provide unstable results in the upper mesosphere, where the small amount of $O_2(a^1\Delta_g)$ present can overestimate the O_3 concentration.

4.3.4 Steady-State Ratio Technique

The other retrieval methods that have been examined are based on a nonlinear relaxation, or ratio, technique. These methods employ an iterative scheme that requires no *a priori* information and use the ratio of measured to modeled $O_2(a^1\Delta_g)$ to estimate the ozone concentrations.

The forward model described in this work produces a set of output $O_2(a^1\Delta_g)$ concentrations, x_i, from a set of input O_3 concentrations, y_i, described by a moderately nonlinear system. Chahine (1970) showed that for a problem where a measurement, y_j, is most strongly affected by the parameter x_i, it is possible to solve iteratively for the parameter x_i by adjusting it by the ratio between the measured and modeled data values,

$$x_i^{(n+1)} = x_i^{(n)} \left(\frac{y_j^{obs}}{y_j^{(n)}} \right). \tag{4.6}$$

Here the ozone concentration at the n^{th} iteration, $x_i^{(n)}$, results in a series of $O_2(a^1\Delta_g)$ concentrations, $y_j^{(n)}$, at this iteration and y_j^{obs} is the measured singlet delta concentration.

The justification for this approach relies on the fact that the weighting function for a given measurement y_j peaks at a specific ozone concentration x_i in this problem. There is a small negative contribution to the $O_2(a^1\Delta_g)$ concentration from ozone at heights above due to Hartley band absorption, but this contribution is very small compared to the contribution of the ozone at the same height as the $O_2(a^1\Delta_g)$ measurement. As a result, the ratio of the measured to modeled $O_2(a^1\Delta_g)$ at each height may be used as a weight to modify the O_3 concentration at that height at each iteration.

This approach is fast, requires no evaluation of weighting functions, and accurately recovers the measured $O_2(a^1\Delta_g)$ within two or three iterations.

4.3.5 Time-Dependent Ratio Technique

The ratio technique presented in the previous section may also be used in a time-dependent retrieval. The goal of this technique is to retrieve the local-noon O_3 profile at each point along the orbit track. This is accomplished by choosing an estimate of the O_3 profile at local noon at the measurement point, and integrating the continuity equation from local noon until the measurement time. The ratio technique, equation (4.6), is then applied to the measured and modeled $O_2(a^1\Delta_g)$ concentrations at the measurement's local time. This process is repeated until the change in the local-noon O_3 concentration is less than some pre-defined value.

This technique arguably provides the best measure of the O_3 concentration as no steady-state assumptions are required. However, the integration of the continuity equation makes it computationally intensive. As well, the effects of dynamics become increasingly important as the model is integrated forward in time.

4.4 Comparison of Techniques

4.4.1 Comparisons of Retrieved O_3 and $O_2(a^1\Delta_g)$

The techniques reviewed in the previous section provide different results for the retrieved O_3 profiles. The retrieved ozone profiles for a latitude of 68° for a June 21, 2003 orbit, obtained using each technique, are shown in Figure 4.8. In this figure two solutions are evident. The time-dependent technique provides characteristically lower O_3 concentration profiles because the non-steady state photochemistry is considered, and the other techniques provide essentially identical results. The time-dependent technique retrieves the O_3 concentrations at local noon at that location, when the ozone concentration is always lowest due to the diurnal variation. The steady-state retrieval techniques obtain characteristically higher concentrations of ozone, since the values are retrieved for the local time at measurement. The main differences between the retrieved O_3 concentrations exist above 65 km, where effects

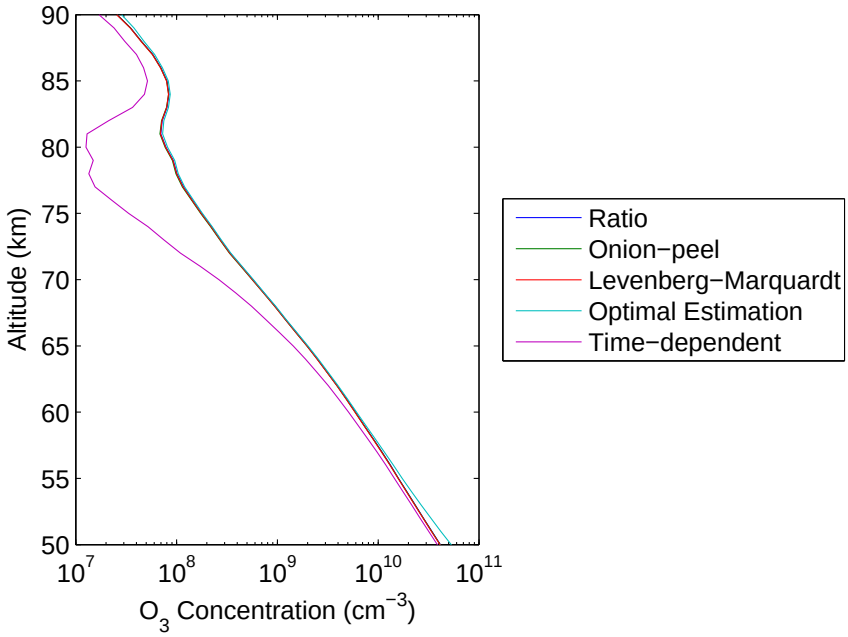

Figure 4.8: Retrieved O_3 concentrations for 68°N on June 21, 2003: comparison of retrieval techniques.

due to dynamical structures can become significant. In this region, the calculated O_3 structures still apply, however the retrieved concentrations will show a larger uncertainty. It is also evident from this figure that the O_3 concentration retrieved by optimal estimation is characteristically higher below 55 km. The the weighted average taken with the *a priori* profile causes this deviation.

The recovered $O_2(a^1\Delta_g)$ concentrations that were obtained from the O_3 profiles shown in Figure 4.8, for each retrieval technique, are shown with the measured $O_2(a^1\Delta_g)$ concentrations in Figure 4.9. It is evident that the results from the five retrieval techniques are very similar. All techniques, apart from the onion-peel algorithm, accurately recover the measured $O_2(a^1\Delta_g)$ profile; the onion-peeled result is systematically higher. This is due to the inherent uncertainty that results from very low $O_2(a^1\Delta_g)$ concentrations near the top of the measurement region. As a

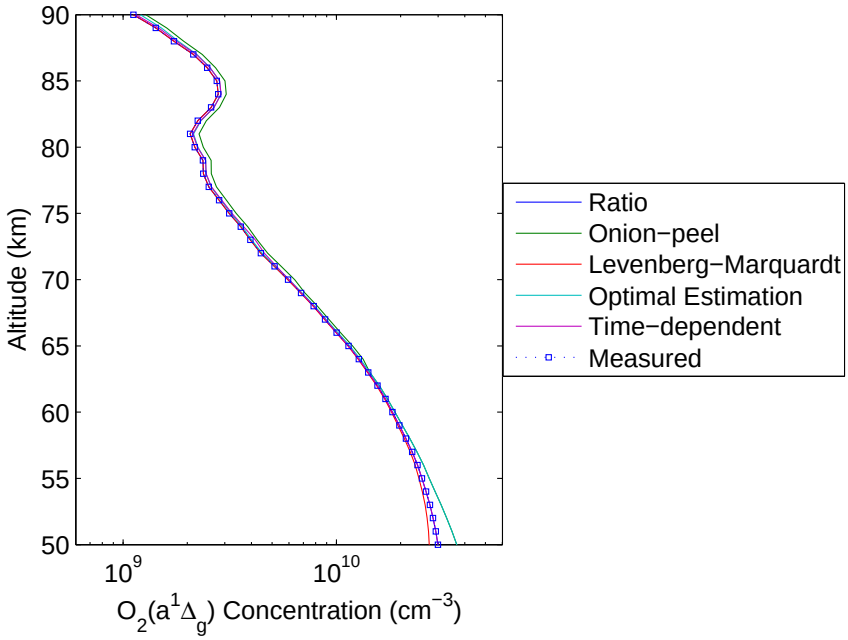

Figure 4.9: Recovered $O_2(a^1\Delta_g)$ concentrations for 68°N on June 21, 2003: comparison of retrieval techniques.

result the technique must work downwards before stabilizing.

4.4.2 Selection of Retrieval Technique

To be selected as a valid retrieval method, a technique must accurately reproduce the measurements by adjusting forward model parameters. In the previous section, it was seen that O_3 profiles retrieved by the Levenberg-Marquardt, steady-state ratio, and time-dependant ratio methods all recovered $O_2(a^1\Delta_g)$ concentrations that were in very good agreement with the measurements. The selection of a retrieval technique depends on a combination of accuracy and speed. A comparison of the speed of the retrieval techniques is shown in Table 4.3. The more computationally-intensive nature of the Levenberg-Marquardt technique prevents it from being used on an operational basis. For this reason, the steady-state and non-steady-state ratio-

Technique	Speed (sec/profile)
Levenberg-Marquardt	7
Optimal estimation	6
Onion-peel	< 1
Nonlinear relaxation	< 1
Time-dependent	50

Table 4.3: Comparison of retrieval techniques.

based techniques are used for performing retrievals. The steady-state ratio technique provides both very accurate recovery of the measured $O_2(a^1\Delta_g)$ concentration, as well as speed in performing retrievals.

4.4.3 Systematic Differences between Ratio-based Retrieval Techniques

It was seen in the previous subsection that the steady-state and non-steady state ratio-based techniques provide retrieved O_3 profiles that are systematically different. The time-dependent technique retrieves values of O_3 that are characteristically lower.

The time-dependent technique must necessarily give the most accurate results as it includes the time-dependent photochemistry. However, the need to integrate the continuity equation prevents it from being an operational method. For this reason, results from the time-dependent technique are used as a baseline retrieval, and the steady-state ratio-based retrievals are used for performing operational retrievals.

4.5 Retrieved O_3 in the Odin Orbit

Once the retrieval technique has been established, retrievals can be performed on an operational orbit-by-orbit basis for the duration of the Odin mission up to the current time.

The average retrieved O_3 from several orbits on June 21, 2003 is shown in Figure 4.10. It should be noted in this figure, and in subsequent two-dimensional plots of ozone, that the false-color scale indicates logarithmic concentrations of O_3 (unless otherwise noted). It is seen in this figure that higher concentrations of ozone are

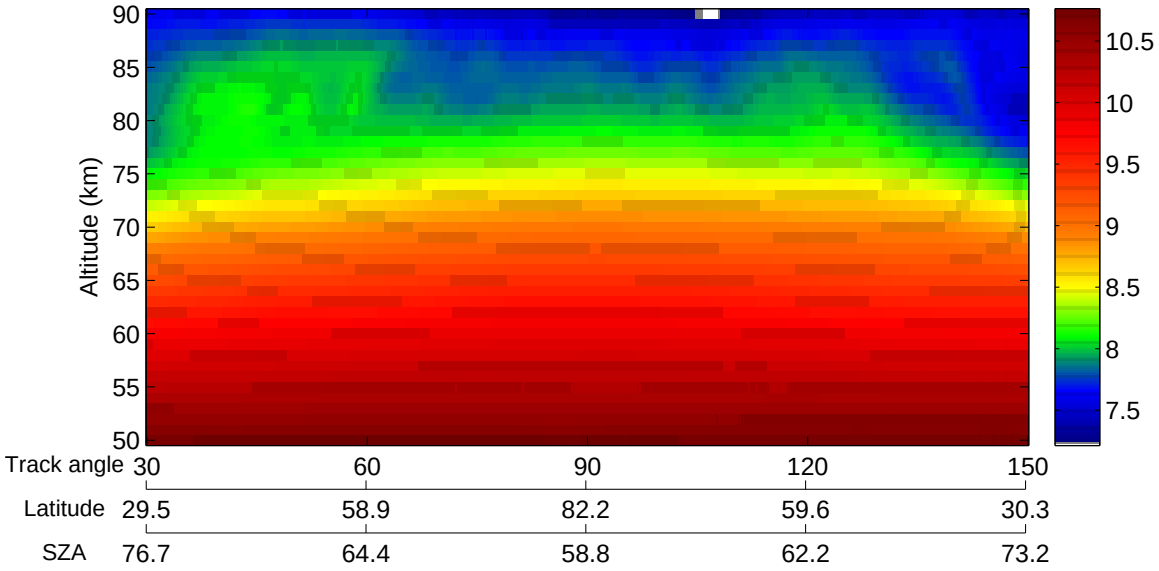

Figure 4.10: Average retrieved O_3 concentrations [$\log_{10}(\mathrm{cm}^{-3})$] for eight orbits on June 21, 2003.

seen at heights near 75 km in the polar region. An additional O_3 structure is seen near 80 km below 60° along the orbit track. In this figure, retrieved O_3 is shown for 30 to 150° along the orbit track as this is the photochemical steady-state region.

Chapter 5

Retrieval Sensitivity and Comparisons

5.1 Introduction

In this chapter the sensitivity of ozone retrievals to the loss coefficients of $O_2(a^1\Delta_g)$ is examined. A preliminary comparison of the retrieved results to those obtained by two other instruments is also presented. It is shown that the use of complementary measurements from another instrument can be used to fix the values of $O_2(a^1\Delta_g)$ loss coefficients used to perform retrievals.

5.2 Retrieval Sensitivity Analysis

In this section the sensitivity of O_3 retrievals to model parameters is discussed. The parameters that most strongly affect retrievals are the kinetic rates for collisional quenching of $O_2(a^1\Delta_g)$ and the Einstein A-value (Mlynczak and Olander, 1995).

5.2.1 Kinetic Reaction Rates

There is presently significant uncertainty associated with the reaction rates for $O_2(a^1\Delta_g)$ quenching by O_2 and N_2. This uncertainty results from choice of the 'accepted' values that are used and from the experimental uncertainty of the coefficients. From the continuity equation, it is expected that a change in the kinetic reaction rates for $O_2(a^1\Delta_g)$ quenching will proportionately change the retrieved concentrations of O_3.

The two sources for quenching coefficients used in the present work are the evaluations from the Jet Propulsion Laboratory (JPL) (Sander *et al.*, 2003) and from the International Union of Pure and Applied Chemistry (IUPAC) (Atkinson *et al.*, 2005). These data evaluations provide comprehensive reviews of the kinetic and photochemical literature, and frequently provide different recommended values for the same reaction. The $O_2(a^1\Delta_g)$ quenching coefficients reported by these sources are shown in Table 5.1. The variance in the retrieved O_3 profile, at a latitude of

Reaction Rate [cm^3/s]	IUPAC (Atkinson *et al.*, 2005)	JPL (Sander *et al.*, 2003)
k_{Δ,O_2}	$3.0 \times 10^{-18}\exp(-200/T)$	$3.6 \times 10^{-18}\exp(-220/T)$
k_{Δ,N_2}	1.4×10^{-19}	1×10^{-20}

Table 5.1: Reported values of O_2 and N_2 quenching coefficients.

68° and a solar zenith angle of 61.5°, that is due to the choice of O_2 quenching coefficient is shown in Figure 5.1. The minimum and maximum profiles that are obtained by considering the experimental uncertainty of the respective coefficients are also shown.

The reported values of N_2 quenching coefficients do not include experimental uncertainties. The variation in retrieved O_3 due to the use of the two N_2 quenching coefficients is shown in Figure 5.2.

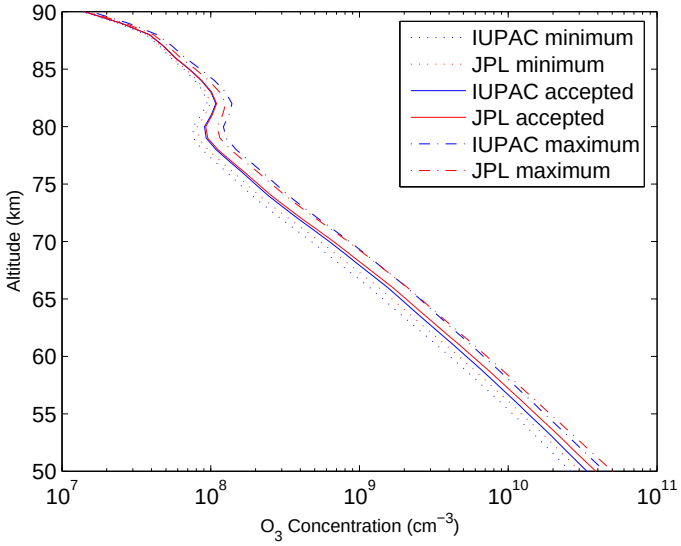

Figure 5.1: Change in retrieved O_3 concentration profile due to choice of O_2 quenching coefficient.

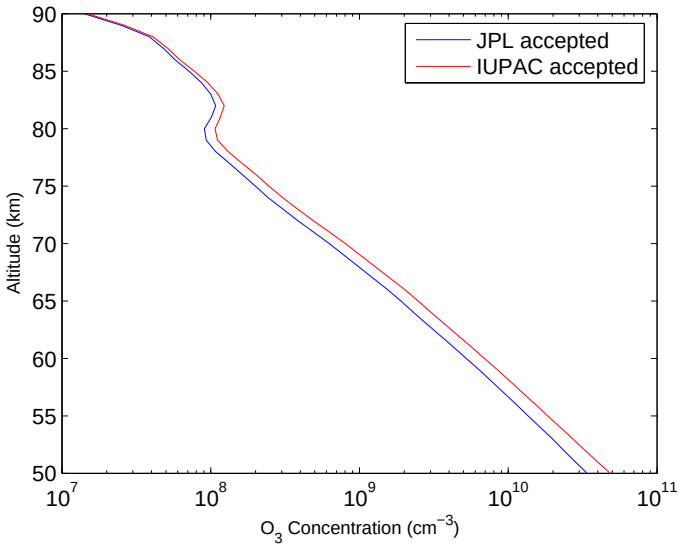

Figure 5.2: Change in retrieved O_3 concentration profile due to choice of N_2 quenching coefficient.

5.2.2 Spontaneous Emission Coefficient

In addition to the variation in retrieved O_3 caused by the choice of quenching coefficients, there is significant variability associated with the OIRA band spontaneous emission coefficient that is used. This coefficient, the Einstein A-value, is a key model parameter as it is used in converting the retrieved $O_2(a^1\Delta_g)$ volume emission rates (VER) to concentrations, and is also involved in loss of $O_2(a^1\Delta_g)$ in the photochemical model. Several reported values are shown in Table 5.2. The A-value

A_Δ [s^{-1}]	Reference
2.58×10^{-4}	Badger *et al.* (1965)
1.47×10^{-4}	Mlynczak and Nesbitt (1995)
2.19×10^{-4}	Newman *et al.* (1999)

Table 5.2: Reported spontaneous emission coefficients for $O_2(a^1\Delta_g)$ radiation.

reported by Badger *et al.* was the accepted value in aeronomy for many years. This was primarily called into question by Mlynczak and Nesbitt, who reported a much smaller value and cited measurements that predate Badger's paper to support their value. More recent studies by Newman *et al.* (1999) and Špalek *et al.* (1999) report A-values that lie between the two extremes, and agree with the Badger value within experimental uncertainty.

The different retrieved O_3 profiles for three values of the spontaneous emission coefficient, A_Δ, are shown in Figure 5.3. It is apparent from this figure that the variation in the A-value causes significant uncertainty in the retrieved O_3 profile.

5.2.3 Selection of Parameters

From all possible combinations of the three $O_2(a^1\Delta_g)$ loss coefficients, two sets can be identified: one that will minimize and one that will maximize the retrieved O_3 for a given set of $O_2(a^1\Delta_g)$ measurements. The retrieved O_3 concentrations from these

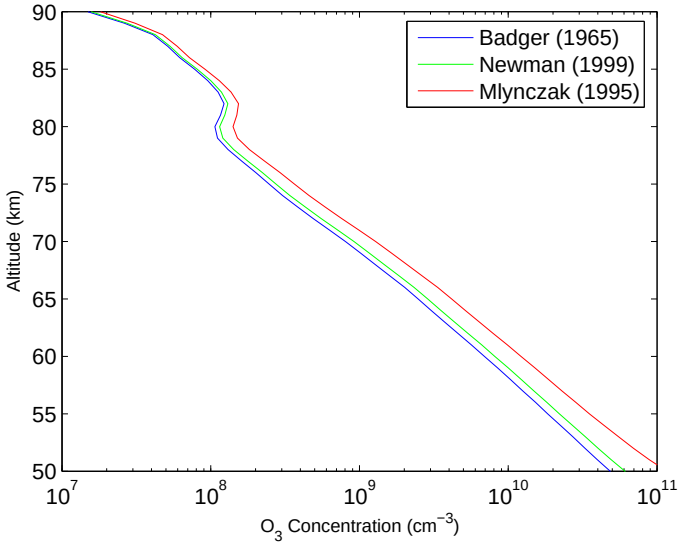

Figure 5.3: Change in retrieved O_3 concentration due to choice of $O_2(a^1\Delta_g)$ Einstein A-value.

sets provide a measure of the uncertainty associated with the retrieved OSIRIS O_3 profiles due to parameter uncertainty. The retrieved concentrations of ozone that result from using each of the sets are shown in Figure 5.4. The retrieved O_3 profile that was found with the selected set of parameters for retrievals is also shown. The calculated uncertainty in the retrieved results agree very well with the uncertainties reported from a previous sensitivity analysis (Sica, 1991).

The selection of the coefficients used in retrievals is based on agreement with concurrent measurements with another instrument. This comparison is presented in Section 5.3.1.

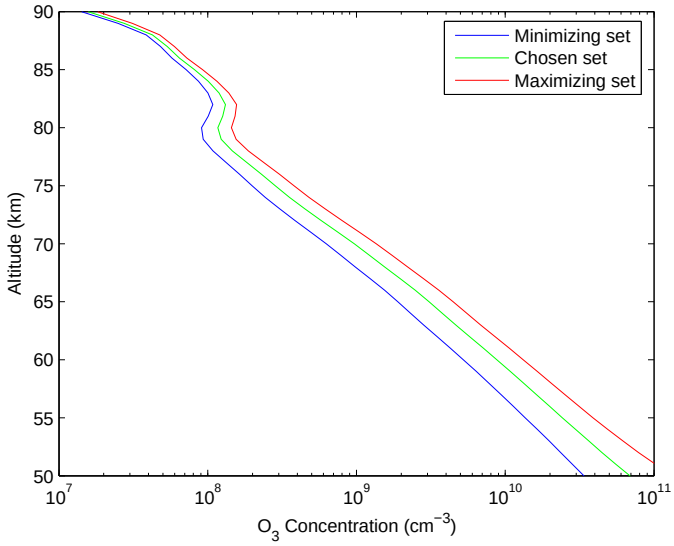

Figure 5.4: Range of retrieved O_3 concentration obtained using the minimizing and maximizing parameter sets.

5.3 Comparisons of Retrieved O_3

5.3.1 Cross-comparison of Optical Spectograph and InfraRed Imaging System Ozone Measurements

The two OSIRIS instruments, the Optical Spectrograph (OS) and the InfraRed Imaging System (IRIS), have coaligned optical axes and make measurements simultaneously. The OS performs retrievals of O_3 from the upper troposphere to the lower mesosphere through radiance measurements in the Chappuis and Hartley bands (Degenstein *et al.*, 2005). The wavelengths used with OS retrievals depend on the dominant absorption feature in a given height range. For the upper stratosphere and lower mesosphere measurements, retrievals are based on Hartley band radiances. Ozone concentrations are retrieved by iterations with a fully spherical radiative transfer model that employs successive orders of scattering.

Spectrograph retrievals are performed up to a height of 60 km, which gives 10 km

of overlap and concurrent measurements with the two instruments. As the measurements are made simultaneously, comparisons may be done between the retrieved O_3 from the two instruments. Also, as OS retrievals are based on direct measurement, they are independent of the rate coefficients involved in $O_2(a^1\Delta_g)$ photochemistry. There is a small sensitivity of these retrievals to the absorption cross sections used; however, this error does not scale the retrieved O_3 proportionately, as is the case with the rate coefficients.

This dual measurement capacity allows for a determination of the best choice of rate coefficients for IRIS retrievals. Many imager observations are made during the course of one spectrograph scan, so comparisons are done by averaging the retrieved IRIS O_3 profiles made during each spectrograph scan, an elapsed time of roughly ninety seconds. A comparison of the retrieved ozone from both instruments at a latitude of 47°N for an orbit on June 21, 2003 is shown in Figure 5.5. There is

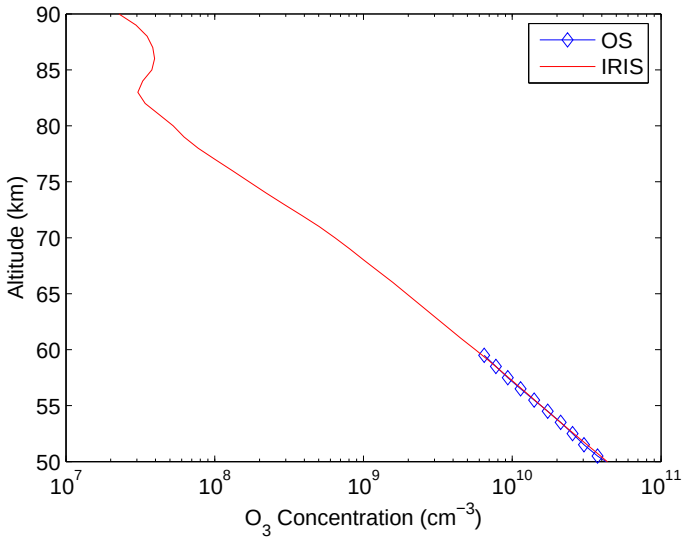

Figure 5.5: Comparison of OS and IRIS retrieved O_3: 47°N, June 21, 2003.

excellent agreement between the measurements made by the two instruments in the overlapping height range. The ozone profiles retrieved within this height range

typically show very little structure, and are characterized by a simple exponential decay up to a height of 75 km. The simple exponential decay characteristically seen in this overlap region readily allows for comparisons between the retrieved results from the two instruments. It should be noted that Von Savigny (2002) and Degenstein *et al.* (2005) performed numerous comparisons of O_3 retrieved from the OS and other instruments, and have found excellent agreement with satellite-based and ozonesonde measurements.

In the overlapping height range, comparisons can be done by plotting the O_3 concentrations at each height from the two instruments against each other. A scatter plot of the retrieved O_3 using the steady-state ratio technique for a June 21, 2003 orbit is shown in Figure 5.6 for the three parameter sets described in Section 5.2.3. This

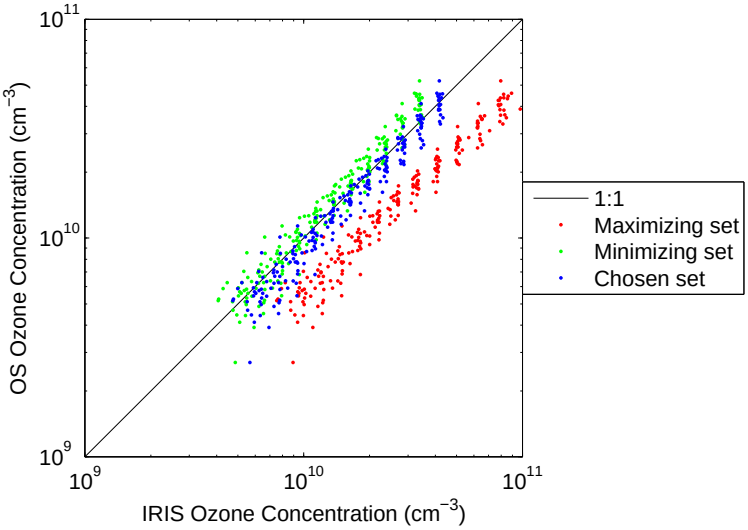

Figure 5.6: Scatter plot of retrieved O_3 from the optical spectrograph and the infrared imaging system.

figure shows excellent agreement between the results retrieved from the two instruments when the correct parameter set is used. A large number of comparisons have been done, and it has been found that the parameters that best match the results

between instruments are a spontaneous emission coefficient of 2.19×10^{-4} s^{-1} (Newman *et al.*, 1999) and O_2 and N_2 quenching coefficients of $3.0 \times 10^{-18}\exp(-200/T)$ and 1.0×10^{-20} cm^{3}s^{-1}, respectively. These are the parameters that are used for all retrievals in this work.

5.3.2 Cross-comparison with SME Measurements

The Solar Mesospheric Explorer (SME) (Thomas *et al.*, 1984) made measurements of the 1.27 μm band with a limb-scanning spectrometer in the stratosphere and mesosphere for a number of years and provided the first global picture of mesospheric O_3 and $O_2(a^1\Delta_g)$.

Some basic comparison can be made between the SME reported average mid-latitude O_3 for the month of June and that retrieved from OSIRIS. The reported mid-latitude ozone profile for June from SME is shown together with the analogous result from OSIRIS in Figure 5.7. It is apparent from this figure that the O_3 concentrations

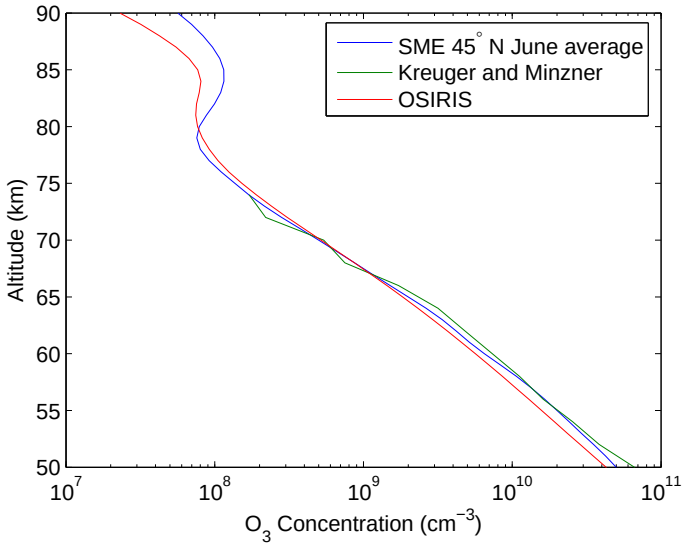

Figure 5.7: Comparison of OSIRIS June average with SME and previous climatological values.

retrieved by OSIRIS are characteristically lower than the SME average.

The retrievals of O_3 concentrations from SME face the difficulties encountered with OSIRIS. Both retrievals are sensitive to the same reaction rates, and small variations in these values can significantly change the retrieved O_3 concentrations. However, the use of cross-comparisons with an independent and concurrent measurement of O_3 provides a useful means for establishing the values of the reaction rates used in the retrieval.

The chemistry used with the reported SME retrievals did not consider the contributions from the A-band transfer, so it is expected that the OSIRIS values should be systematically lower than those obtained by SME.

5.4 Tertiary Mesospheric O_3 Enhancement

A tertiary ozone maximum has been observed with OSIRIS in the northern and southern hemispheres. This layer appears consistently as an enhancement to the retrieved $O_2(a^1\Delta_g)$ concentrations in both hemispheres for several months following each hemisphere's winter-to-summer equinox. An example of the enhancement seen in the $O_2(a^1\Delta_g)$ concentrations is shown in Figure 5.8. The peak appears as a 'finger' that becomes distinct from the primary maximum near 70 km. The height of the layer's peak concentration changes with latitude, from above 80 km at low latitudes to 68 km near the pole. The change in the peak height can be attributed to differences in optical depth between ultraviolet regions that offset the production and loss mechanisms of odd-oxygen, O_x. The feature appears as a strong enhancement throughout a daily average of $O_2(a^1\Delta_g)$, eliminating the possibility that this is an effect related to tidal activities.

The existence of a secondary O_3 maximum near 85 km was first discussed by Hays and Roble (1973). The secondary (85 km) peak was found to result from increased production of atomic oxygen by photolysis in the Schumann-Runge bands and continuum. The depth of the O_3 minimum near 75 km between the primary

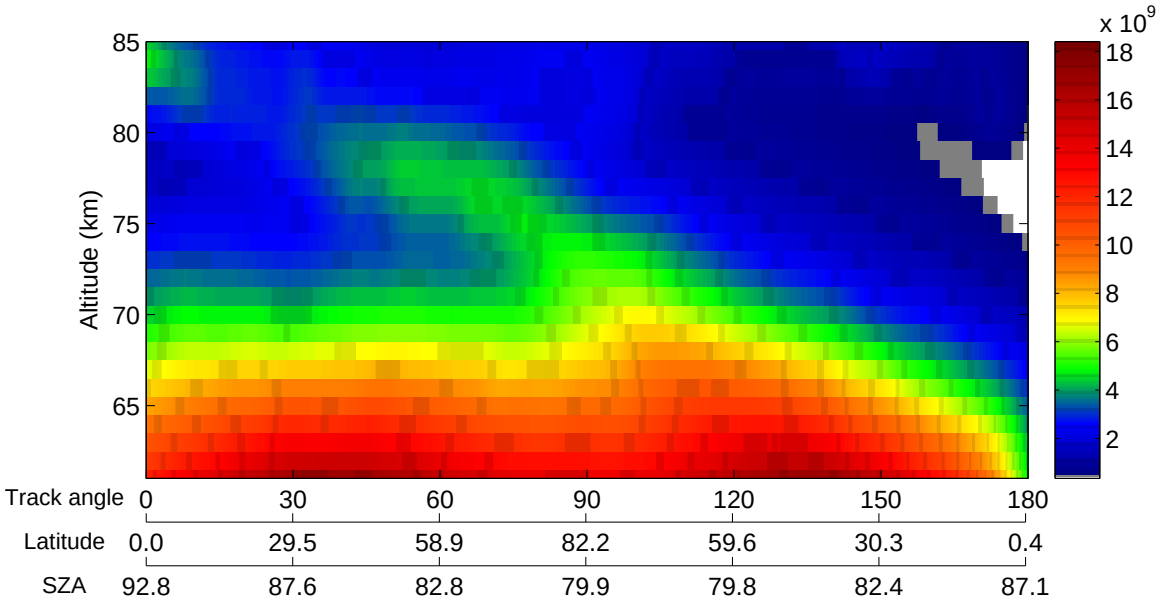

Figure 5.8: $O_2(a^1\Delta_g)$ observations showing tertiary enhancement: average of ten orbits on April 10, 2002.

and secondary peaks depends on the catalytic destruction rates of O_x by odd hydrogen species ($HO_x = H + OH + HO_2$). Marsh *et al.* (2001) suggested that as odd-hydrogen species are produced primarily by water vapor photolysis, at wavelengths below 185 nm, large optical depths for these wavelengths will result in an increase in odd oxygen. If the atmosphere is less optically thick to UV wavelengths above 185 nm, production of O_x by the Schumann-Runge system continues, and its ongoing production is not matched by the typical corresponding losses. Marsh *et al.* also provided modeling work that suggested this is a valid production mechanism and gave several examples of single detections by the Microwave Limb Sounder (MLS) and CRyogenic Infrared Spectrometers and Telescopes for the Atmosphere (CRISTA) instruments.

The global picture of the enhancement provided by OSIRIS, showing both the spatial extent of this enhancement and its long-lived nature, provides a new insight

into the photochemistry of mesospheric ozone. The ozone concentrations retrieved from the $O_2(a^1\Delta_g)$ measurements shown in the previous figure are shown in Figure 5.9. This shows a significant enhancement in the O_3 concentration in the region

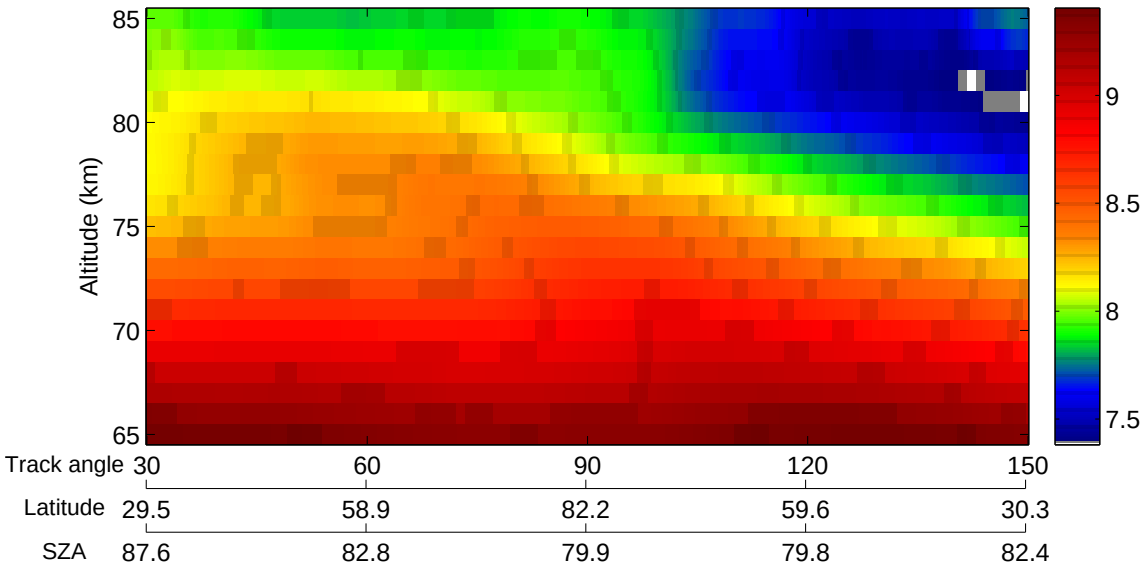

Figure 5.9: Retrieved O_3 concentration $\log_{10}(\mathrm{cm}^{-3})$ showing tertiary enhancement: average of ten orbits on April 10, 2002.

where the 'finger' structure was seen in Figure 5.8. Enhanced O_3 concentrations are evident between 70 and 80 km on the ascending node segment. The change in the tertiary peak height with latitude agrees with the suggestions by Marsh *et al.*, as the critical optical depth occurs at lower measurement heights when the sun is higher. This work has recently been reported by Degenstein *et al.*, 2005.

5.5 Polar Maps of Mesospheric Ozone

Successive orbits of retrieved O_3 can be combined and binned to give maps of mesospheric ozone at a given height. Interesting features have been observed in the

retrieved O_3 concentrations when the vertical sum of the 85 km secondary peak is mapped. The north pole map of the retrieved 80-90 km O_3 columns from ten orbits on June 21, 2003 are shown in Figure 5.10. A structure that is possibly indicative

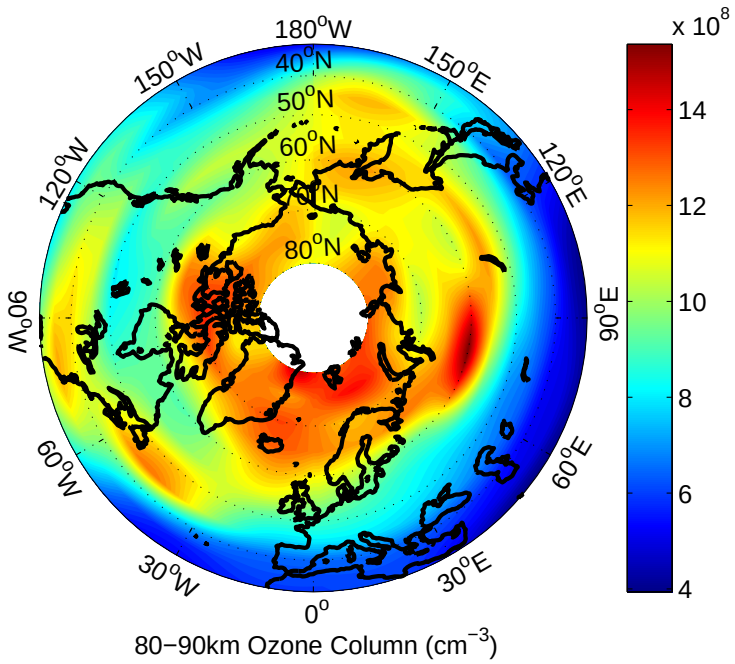

Figure 5.10: Retrieved sum of O_3 concentrations [cm^{-3}] from 80-90 km for June 21, 2003.

of wavenumber-4 dynamical activity is evident in this figure, with maxima in O_3 concentration near 60°N at longitudes of 105°W, 15°W, 75°E, and 165°E. Similar maps can be made for other altitude regions.

5.6 Summary

The sensitivity of O_3 retrievals to key model parameters has been presented in this chapter, and it has been shown that experimental uncertainty in the $O_2(a^1\Delta_g)$ quenching coefficients and A-values can cause significant uncertainty in the retrieved

O_3 profiles. Preliminary comparisons of retrieved O_3 with the results of other instruments have shown good agreement. Comparisons of ozone concentrations retrieved in this work with concurrent measurements have shown excellent agreement, and have given an independent, complementary measurement that is not sensitive to the same parameters.

A database of retrieved mesospheric ozone has been produced for the course of the Odin mission to date.

Chapter 6

Summary and Conclusions

6.1 Summary of the Present Work

In the present work a photochemical software model that models the expected concentrations of excited-state molecular oxygen for a given set of ozone concentrations has been developed. This model has been run and tested in a variety of cases, and has been found to accurately capture the photochemical features observed with the OSIRIS instrument on the Odin satellite.

This model has also been used in conjunction with a nonlinear relaxation retrieval technique to retrieve concentrations of mesospheric ozone from OSIRIS measurements of excited-state molecular oxygen. The retrieval technique very accurately matches the recovered, modeled concentrations of excited-state molecular oxygen to the measurements. Preliminary comparisons have been performed with other instruments making similar measurements, and it has been found that the ozone concentrations retrieved in this work are in excellent agreement with the results obtained by other instruments.

Due to the measurement uncertainties in kinetic rate coefficients used in retrievals, there is an associated error in the retrieved ozone concentrations. Comparisons have been made with concurrent ozone measurements from an instrument

whose retrievals are insensitive to these reaction rates, and excellent agreement have been found with the ozone concentrations obtained in this work. This comparison method also provides a means to further study the values of these coefficients.

6.2 Recommendations for Future Work

There is an obvious need to extend the comparison of the retrieved ozone from the InfraRed Imaging System with contemporary instruments that measure mesospheric ozone. The comparison of retrieved results with instruments that use different measurement techniques is critical in the evaluation of retrievals and in validation of a data product. However, it is beyond the scope of the present work. The Microwave Limb Sounder (MLS) on the Aura spacecraft views microwave emissions to retrieve ozone densities, and provides extensive global coverage. GOMOS (Global Ozone Monitoring by Occultation of Stars) on the Envisat satellite gives spatially limited but very high-resolution ozone measurements that would be useful for comparisons of structures seen in retrieved results. In addition, MIPAS (Michelson Interferometer for Passive Atmospheric Sounding) on Envisat, a Fourier transform limb spectrometer, provides another complementary measurement. This comparison work would also have the benefit of establishing values for the quenching coefficients for singlet delta molecular oxygen.

The model developed in this work does not simultaneously solve for mesospheric odd-hydrogen species. However, such a model has been developed and should be incorporated in future work.

Further work is also necessary in the development of a time-dependent retrieval. The present work employs a steady-state retrieval technique that assumes that the O_2 singlet delta concentration has not changed by more than a few percent during the measurement time. A significant portion of the ascending and descending nodes of the Odin orbit are in photochemical non-steady state conditions, where a fully time-dependent retrieval is required to exploit the OSIRIS data fully.

6.3 Conclusion

A database of mesospheric ozone concentrations retrieved from measurements made by the OSIRIS InfraRed Imaging System has been produced in this work. This database provides ozone concentrations throughout the course of the Odin mission, within the height and latitude ranges specified in Tables 4.6 and 4.7.

References

Atkinson, R., D.L. Baulch, R.A. Cox, J.N. Crowley, R.F. Hampson, Jr, R.G. Hynes, M.E. Jenkin, J.A. Kerr, M.J. Rossi, and J. Troe: "Summary of Evaluated Kinetic and Photochemical Data for Atmospheric Chemistry IUPAC Subcommittee on Gas Kinetic Data Evaluation for Atmospheric Chemistry", `http://www.iupac-kinetic.ch.cam.ac.uk/summary/IUPACsumm_web_latest.pdf`, 2005.

Badger, R.M., A.C. Wright, and R.F. Whitlock: "Absolute intensities of the discrete and continuous absorption bands of oxygen gas at 1.26 and 1.065μ and the radiative lifetime of the $a^1\Delta_g$ state of oxygen", *J. Chem. Phys.*, **43**, 4345, 1965.

Bantle, M., E.J. Llewellyn, and B.H. Solheim: "Measurement of $O_2(a^1\Delta_g)$ Emission in a Total Solar Eclipse", *J. Atmos. Terr. Phys.*, **46**, 265, 1984.

Barth, C.A., D.W. Rusch, R.J. Thomas, G.H. Mount, G.J. Rottman, G.E. Thomas, R.W. Sanders, and G.M. Lawrence: "Solar Mesospheric Explorer: Scientific Objectives and Results", *Geophys. Res. Letters*, **10**, 237, 1983.

Bates, D.R. and M. Nicolet: "The photochemistry of atmospheric water vapour", *J. Geophys. Res.* **55**, 301, 1950.

Bovensmann, H., J.P. Burrows, M. Buchwitz, J. Frerick, S. Noel, V.V. Rozanov, K.V.Chance, and A.P.H. Goede: "SCIAMACHY: Mission objectives and measurement modes", *J. Atmos. Sci.*, **56**, 127, 1999.

Chahine, M.T.: "Inverse Problems in Radiative Transfer: Determination of Atmospheric Parameters", *J. Atmos. Sci.*, **27**, 960, 1970.

Chapman, S.: "A Theory of Upper-Atmospheric Ozone", *Mem. Royal Met. Soc.* **3**,

26, 103, 1930.

De More, W.B., S.P. Sander, C.J. Howard, A.R. Ravishankara, D.M. Golden, C.E. Kolb, R.F. Hampson, M.J. Kurylo, and M.J. Molina: "Chemical Kinetics and Photochemical Data for Use in Stratospheric Modeling, Evaluation Number 12", NASA, 2003.

Degenstein, D.A., E.J. Llewellyn, and N.D. Lloyd: "Volume emission rate tomography from a satellite platform", *Appl. Optics*, **42**, 8, 1441, 2003.

Degenstein, D.A., A.E. Bourassa, R.L. Gattinger, and E.J. Llewellyn: "Retrieval of vertical ozone profiles with OSIRIS limb scattered spectra from 10 to 60 kilometres", *J. Atmos. Sci.*, submitted, 2005.

Degenstein, D.A., R.L. Gattinger, N.D. Lloyd, A.E. Bourassa, J.T. Wiensz and E.J. Llewellyn: "Observations of a Tertiary Ozone Peak in the Mesosphere", *J. Atmos. Space Terr. Phys.*, (in press), 2005.

Ellis, J.W. and H.O. Kneser: *Z. Phys.*, **86**, 583, 1933.

Evans, W.F.J.: Ph.D. Thesis, University of Saskatchewan, 1967.

Evans, W.F.J., D.M. Hunten, E.J. Llewellyn, and A. Vallance Jones: "Altitude Profile of the Infrared Atmospheric System of Oxygen in the Dayglow", *J. Geophys. Res.*, **73**, 9, 2885, 1968.

Fabry, C. and H. Buisson: *J. Physique*, **2**, 196, 1913.

Fabry, C. and H. Buisson: *J. Physique*, **3**, 197, 1921.

Hartley, W.N.: *Chem. News*, **42**, 268, 1880.

Haslett, J.C., L.R. Megill, and H.I. Schiff: "Rocket measurement of $O_2(a^1\Delta_g)$", *Can. J. Phys.*, **47**, 2351, 1969.

Hays, P.B. and R.J. Roble: "Observation of mesospheric ozone at low latitudes", *Planet. Space Sci.*, **21**, 2, 273, 1973.

Hedin, A.E.: "Extension of the MSIS thermosphere model into the middle and lower atmosphere.", *J. Geophys. Res*, **96**, A2, 1159, 1991.

Herzberg, G: "Photography of the Infra-Red Solar Spectrum of Wavelength 12,900 Å.", *Nature*, **133**, 759, 1934.

Herzberg, G: Molecular Spectra and Molecular Structure: Volume I - Spectra of Diatomic Molecules. Krieger Publishing Company, 1989.

Kockarts, G.: "Penetration of solar radiation in the Schumann-Runge bands of molecular oxygen: a robust approximation", *Ann. Geophysicae*, **12**, 1207, 1994.

Krueger, A.J. and R.A. Minzner: "A mid-latitude ozone model for the 1976 U.S. standard atmosphere", *J. Geophys. Res.*, **81**, 4477, 1976.

Kurucz, R.L.: *The solar irradiance by computation*, Proc. 17^{th} Annual Conference Transmission Models, Phillips Laboratory, Hanscom AFB, PL-TR-95-2060. G.P. Anderson, et al. Eds. PP, 333, 1995.

Llewellyn, E.J., W.F.J. Evans, A. Vallance Jones, and D.M. Hunten: "The Altitude Profiles of the (0-0) Band of the ($^1\Delta_g - ^3\,\Sigma_g^-$) System of Oxygen in the Day and Twilight Airglow", *Trans. Amer. Geophys. Union*, **48**, 71, 1967.

Llewellyn, E.J., N.D. Lloyd, D.A. Degenstein, R.L. Gattinger, S.V. Petelina, A.E. Bourassa, J.T. Wiensz, E.V. Ivanov, I.C. McDade, B.H. Solheim, J.C. McConnell, C.S. Haley, C. von Savigny, C.E. Sioris, C.A. McLinden, W.F.J. Evans, E. Puckrin, K. Strong, V. Wehrle, R.H. Hum, D.J.W. Kendall, J. Matsushita, D.P. Murtagh, S. Brohede, J. Stegman, G. Witt, G. Barnes, W.F. Payne, L. Pich, K. Smith, G. Warshaw, D.-L. Deslauniers, P. Marchand, E.H. Richardson, R.A. King, I. Wever, W. McCreath, E. Kyrl, L. Oikarinen, G.W. Leppelmeier, H. Auvinen, G. Mgie, A. Hauchecorne, F. Lefvre, J. de La No, P. Ricaud, U. Frisk, F. Sjoberg, F. von Schele and L. Nordh: "The OSIRIS Instrument on the Odin Spacecraft", *Can. J. Phys.*, **82**, 411, 2004.

Lloyd, N.D. and E.J Llewellyn: "Deconvolution of blurred images using photon counting statistics and maximum probability", *Can. J. Phys.*, **67**, 89, 1989.

López-González, M.J., J.J. López-Moreno, M.A. López-Valverde, and R. Rodrigo: "Behaviour of the O_2 infrared atmospheric $(0,0)$ band in the middle atmosphere during evening twilight and at night", *Planet. Space Sci.*, **37**, 1, 61, 1989.

Marsh, D., A. Smith, G. Brasseur, M. Kaufmann, and K. Grossmann: "The exis-

tence of a tertiary ozone maximum in the high-latitude middle mesosphere", *Geophys. Res. Lett.*, **28**, 24, 4531, 2001.

McDade, I.C. and E.J. Llewellyn: "Inversion techniques for recovering two-dimensional distributions of auroral emission rates from tomographic rocket photometer measurements", *Can. J. Phys.*, **69**, 1059, 1991.

McPeters, R.D., G.J. Labow, and B.J. Johnson: "A satellite-derived ozone climatology for balloonsonde estimation of total ozone", *J. Geophys. Res.*, **102**, D7, 8875, 1997.

Mlynczak, M.G., S. Solomon, and D.S. Zaras: "An updated model for $O_2(a^1\Delta_g)$ concentrations in the mesosphere and lower thermosphere and implications for remote sensing of ozone", *J. Geophys. Res.*, **98**, D10, 18648, 1993.

Mlynczak, M.G. and D.J. Nesbitt: "The Einstein coefficient for spontaneous emission of the $O_2(a^1\Delta_g)$ state", *Geophys. Res. Lett.*, **22**, 1, 381, 1995.

Mlynczak, M.G. and D.S. Olander: "On the utility of the molecular oxygen dayglow emissions as proxies for middle atmospheric ozone", *Geophys. Res. Lett.*, **22**, 11, 1377, 1995.

Newman, S.M., I.C. Lane, A.J. Orr-Ewing, D.A. Newnham, and J. Ballard: "Integrated absorption intensity and Einstein coefficients for the $O_2(a^1\Delta_g) \rightarrow O_2(X^3\Sigma_g^-) + h\nu(1.27\mu m)$ (0,0) transition: A comparison of cavity ringdown and high resolution Fourier transform spectroscopy with a long-path absorption cell", *J. Chem. Phys.*, **110**, 22, 10749, 1999.

Noxon, J.F. and A. Vallance Jones: "Observation of the $(0,0)$ Band of the $a^1\Delta_g - X^3\Sigma_g^-$ System of Oxygen in the Day and Twilight Airglow", *Nature*, **196**, 157, 1962.

Noxon, J.F. and T.P. Markham: "Oxygen spectra in dayglow, twilight, and during an eclipse ", *J. Geophys. Res.*, **68**, 6059, 1963.

Press, W.H., S.A. Teukolsky, W.T. Vetterling, and B.P. Flannery: Numerical Recipes in C: The Art of Scientific Computing, Second Edition, Cambridge University Press, 1992.

Rodgers, C.D.: "Retrieval of Atmospheric Temperature and Composition From Re-

mote Measurements of Thermal Ratiadion", *Rev. Geophys and Space Phys.*, **14**, 4, 609, 1976.

Rothman, L.S., A. Barbe, D. Chris Benner, L.R. Brown, C. Camy-Peyret, M.R. Carleer , K. Chance, C. Clerbaux ;g, V. Dana, V.M. Devi, A. Fayt, J.-M. Flaud, R.R. Gamache, A. Goldman, D. Jacquemarta, K.W. Jucks, W.J. Lafferty, J.-Y. Mandin, S.T. Massie, V. Nemtchinov, D.A. Newnham, A. Perrin, C.P. Rinsland, J. Schroeder, K.M. Smith, M.A.H. Smith, K. Tang, R.A. Toth, J. Vander Auwera, P. Varanasi, and K. Yoshino: "The HITRAN molecular spectroscopic database: edition of 2000 including updates through 2001", *J. Quant. Spec. Rad. Tran.*, **82**, 5, 2003.

Russell, J.M., M.G. Mlynczak, L.L. Gordley, J.J. Tansock, and R.W. Esplin: "Overview of the SABER experiment and preliminary calibration results", *Proc. SPIE*, **3756**, 277, 1999.

Sander, S.P., R.R. Friedl, A.R. Ravishankara, D.M. Golden, C.E. Kolb, M.J. Kurylo, R.E. Huie, V.L. Orkin, M.J. Molina, G.K. Moortgat, and B.J. Finlayson-Pitts: "Chemical Kinetics and Photochemical Data for Use in Atmospheric Studies, Evaluation Number 14", *JPL Publ.*, 02-25, 2003.

Sica, R.J.: "Inferring middle-atmospheric ozone height profiles from ground-based measurements of molecular oxygen emission rates, I: Model description and sensitivity to inputs", *Can. J. Phys.*, **69**, 1069, 1991.

Špalek, O., J. Kodymová, P. Stopka, and I. Miček: "Experimental verification of the Einstein A-coefficient used for evaluation of $O_2(^1\Delta_g)$ concentration in the chemical oxygeniodine laser", *J. Phys. B: At. Mol. Opt. Phys.*, **32**, 4, 1885, 1999.

Thomas, R.J., C.A. Barth, G.J. Rottman, D.W. Rusch, G.H. Mount, G.M. Lawrence, R.W. Sanders, G.E. Thomas, and L.E. Clemens: "Ozone density distribution in the mesosphere (50-90 km) measured by the SME limb scanning near infrared spectrometer", *Geophys. Res. Lett.*, **10**, 4, 245, 1983.

Thomas, R.J., C.A. Barth, D.W. Rusch, and R.W. Sanders: "Solar Mesosphere Explorer Near-Infrared Spectrometer: Measurements of 1.27 μm Radiances and the Interference of Mesospheric Ozone", *J. Geophys. Res.*, **89**, D6, 9569, 1984.

Vallance Jones, A. and R.L. Gattinger: "The seasonal variation and excitation mechanism of the 1.58 μm $^1\Delta_g - ^3\Sigma_g^-$ twilight airglow band", *Planet. Space Sci.*, **11**, 961,

1963.

Vallance Jones, A. and R.L. Gattinger: "The $^1\Delta_g - ^3\Sigma_g^+$ O_2 bands in the twilight and day airglow", *Planet. Space Sci.*, **14**, 1, 1966.

von Savigny, C.: Ph.D. Thesis, York University, 2002.

Wood, H.C.: Ph.D. Thesis, University of Saskatchewan, 1972.

Zhao, X. and R.P. Turco: "Photodissociation parameterization for stratospheric photochemical modeling", *J. Geophys. Res.*, **102**, D8, 9447, 1997.